Effective synthesis route of renewable activated biocarbons adsorbent for high CO<inf>2</inf>, CH<inf>4</inf>, H<inf>2</inf>, N<inf>2</inf>,

Fuel 374 (2024) 132462

Contents lists available at ScienceDirect

Fuel

journal homepage: www.elsevier.com/locate/fuel

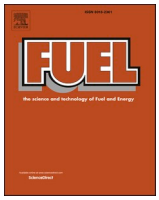

Full Length Article

Effective synthesis route of renewable activated biocarbons adsorbent for high CO_2, CH_4, H_2, N_2, C_2H_4 gas storage and CO_2/N_2, CO_2/CH_4, CO_2/H_2, C_2H_4/CH_4 selectivity

Jarosław Serafin [a,*], Bartosz Dziejarski [b,c,d,*], Paola Rodríguez-Estupiñán [e], Valentina Bernal Fernández [e], Liliana Giraldo [f], Joanna Sreńscek-Nazzal [g], Beata Michalkiewicz [g], Juan Carlos Moreno-Piraján [e]

[a] Department of Inorganic and Organic Chemistry, University of Barcelona, Martí i Franquès, 1-11, 08028 Barcelona, Spain
[b] Faculty of Environmental Engineering, Wroclaw University of Science and Technology, 50-370 Wroclaw, Poland
[c] Department of Space, Earth and Environment, Division of Energy Technology, Chalmers University of Technology, SE-412 96 Gothenburg, Sweden
[d] Department of Chemistry and Chemical Engineering, Division of Energy and Materials, Chalmers University of Technology, SE-412 96 Gothenburg, Sweden
[e] Chemistry Department, Faculty of Science, Universidad de Los Andes, Cra 1 N° 18A – 12, 111711 Bogota, Colombia
[f] Chemistry Department, Faculty of Science, Universidad Nacional de Colombia, Carrera 45 # 26-85, 111321 Bogota, Colombia
[g] West Pomeranian University of Technology, Szczecin, Faculty of Chemical Technology and Engineering, Department of Catalytic and Sorbent Materials Engineering, Piastów Ave. 42, 71-065 Szczecin, Poland

ARTICLE INFO

Keywords:
Fern leaves
Activated carbon
Bioconversion
Greenhouse gases
Gas storage

ABSTRACT

This study explores the feasibility of producing activated carbons (ACs) from abundant fern leaves to enhance their adsorption capabilities. The process involves activation with H_3PO_4 followed by thermal conversion at temperatures ranging from 700 to 900 °C. Adsorption isotherms for CO_2, CH_4, H_2, N_2, and C_2H_4 were systematically measured at 25 °C under pressures up to 45 bar for all specimens. These data formed the basis for calculating the separation selectivity of CO_2/N_2, CO_2/CH_4, CO_2/H_2, and C_2H_4/CH_4 at various pressures. ACs synthesized at 800 °C (FERN800) exhibited superior characteristics, including a specific surface area of 438 m^2/g, a total pore volume of 0.300 cm^3/g, and a micropore volume of 0.236 cm^3/g. This resulted in significant gas uptake values: 4.21 mmol/g for CO_2, 3.14 mmol/g for CH_4, 1.19 mmol/g for H_2, 2.04 mmol/g for N_2, and 3.36 mmol/g for C_2H_4, at 25 °C and 45 bar. The research demonstrates the potential of fern-derived ACs for high-pressure gas adsorption, particularly in mitigating greenhouse gas emissions and advancing gas separation technologies for applications such as flue gas treatment (post-combustion), syngas production (pre-combustion), biogas upgrading, and hydrocarbon mixtures. Notably, ACs showed a high selectivity of 146 for CO_2 over N_2 at 1 bar in flue gas containing 15 % CO_2, and a selectivity of 90 for CO_2 over H_2 at 1 bar. ACs produced from fern leaves activated by H_3PO_4 also show promise in capturing CO_2 from biogas and natural gas, as well as C_2H_4 from natural gas. Additionally, the calculated cost of producing 1 kg of the AC was found to be 2.45 € (19 CNY), positioning it competitively in the market. This research highlights the innovative use of fern-derived ACs as effective and sustainable adsorbents in various environmental and industrial applications.

1. Introduction

Gas storage and separation are pivotal components in the optimization of various applications, ranging from mobile technologies [1,2] to the improvement of biogas processes [3,4]. The practical implementation of technologies designed for the storage of CO_2, CH_4, N_2, and H_2 gases, along with the separation of CO_2/CH_4 and CO_2/N_2, is widespread across diverse large-scale industrial operations. These applications encompass solid-state hydrogen storage [5,6], hydrogen-fueled vehicles equipped with fuel cells [7,8], natural gas purification procedures [9,10], and the effective capture of carbon dioxide from flue gases [11–14].

The growth in greenhouse gas emissions (GHGs) is one of the world's most significant environmental challenges today [15]. The continuous

* Corresponding authors.
E-mail addresses: jaroslaw.serafin@qi.ub.edu (J. Serafin), bartoszd@chalmers.se (B. Dziejarski).

https://doi.org/10.1016/j.fuel.2024.132462
Received 20 March 2024; Received in revised form 23 June 2024; Accepted 7 July 2024
Available online 15 July 2024

soaring of GHG level in the atmosphere is largely driven by a variety of causes, the most prominent of which are the expansion of human populations, rapid industrialization, the expansion of transportation networks, the clearing of forests, and the expansion of agricultural land [16]. Despite a broaden awareness of the need to decrease GHGs emissions, many governments throughout the globe have been hesitant to act. To accomplish the goals of many policies to mitigate climate change, transitioning to a low-carbon economy and reducing emissions need global coordination and collaboration to address the problem [17]. According to the Intergovernmental Panel on Climate Change (IPCC), the concentration of greenhouse gases in the atmosphere has increased by more than 40 % since preindustrial times [18]. This undesirable phenomenon causes rising sea levels, melting glaciers and ice caps, and more frequent and severe weather events such as hurricanes, droughts, and heatwaves [19]. Unfortunately, the latest report from the International Energy Agency (IEA) confirms that the current trend will use up the allowed future emissions for limiting anthropogenic warming to 1.5 °C.

The primary greenhouse gases are carbon dioxide (CO_2), methane (CH_4), nitrous oxide (N_2O) and fluorinated gases. CO_2 is the most abundant one and is primarily emitted through the burning of fossil fuels, such as of oil, natural gas, and coal for energy production. In 2022, global energy-related CO_2 emissions were estimated at over 36.8 Gt, where the power sector being the largest emitter with 14.65 Gt of global CO_2 emissions. The industry sector represented 9.15 Gt, transport was responsible for 7.98 Gt and buildings accounting for 2.97 Gt [3]. The remaining emissions came from agriculture, forestry, and other land use. On the other hand, with worldwide emissions reaching 4.0 Gt of CO_2-eq in the same year, methane is the second-largest contributor to climate change after carbon dioxide [3,20]. It comes mainly from natural sources, such as wetlands, as well as human activities such as livestock farming, and landfills [21], and mainly from onshore oil and gas production, or steam coal production [3]. What is more, methane tends to lead to global warming which is 84 times stronger than carbon dioxide over a period of 20 years, and its effect is 28 times more severe over a period of 100 years [22]. For nitrogen oxides, the emission values in 2022 were equal to 0.3 Gt of CO_2-eq.

In view of the above, the emerging accumulation of greenhouse gases because of enormous industry development in the global economy, as well as the growing search of the scientific community for transition to clean and adaptable energy carriers (i.e., hydrogen), has led to the search for technologies that allow for addressing the demands of these two critical challenges. Currently, adsorption is extensively reported as one of the most attractive options for mentioned issues, due to the versatility of its assembly, as well as the control over the properties of the material and the adsorption system, including the surface chemistry of the solid and its textural design, temperature, and composition of the process, which can influence the selectivity towards particular component in the gas mixture. Therefore, adsorption allows not only effective capture of GHGs from large stationary emitters, but also safe, compact, lightweight, and cost-effective storage of future fuels [23]. Compared with different adsorbents, activated carbons (ACs) are highly effective materials and are widely used in many applications due to their superior adsorption capabilities [24]. ACs have several advantages that make them a preferred choice for carbon reduction and other environmental applications, including the inexpensive and straightforward process of production from biomass residues, or industrial wastes [25–27]. Furthermore, the unique properties of ACs, which can be customized by adjusting the pore size distribution, surface area, or chemical properties [28], make them a superior choice in the development of climate mitigation projects that have great potential for development on a commercial scale.

Recent research has shown that fern-derived activated carbons have been shown to have superior adsorption properties and unique structure compared to other AC materials, making them an attractive option for preventing climate change [29–32]. Generally, ferns are representatives of pteridophyte plants, which are vascular plants and reproduce by spores. They are an abundant and readily available plant species that have been around on Earth for more than 300 million years [33], which can be found in many different environments, including forests, wetlands, and deserts, or with a higher incidence in tropical areas [34]. They are also rich in cellulose and lignin, which are the primary constituents for ACs synthesis. Furthermore, ferns also possess a high biomass production rate and are considered one of the most efficient photosynthetic plant groups [35], providing a renewable and sustainable source of ACs. Consequently, fern-based ACs, as products of a well-controlled carbonization process, can be widely accepted as a part of the modern agenda to recycle organic by-products and waste and to utilize various environmentally friendly approaches.

The adsorption of CO_2, CH_4, H_2, and N_2 was investigated, with a particular emphasis on the selectivity of CO2 adsorption. This focus was chosen due to the significance of these gases in the composition of natural gas, flue gases, syngas, and biogas. Concentrations of CO2 vary from 5 to 50 %: natural gas (1–10 %) flue gases (15–20 %), syngas (8–20 %), and biogas (30–50 %) [36].

In addition to CO_2 capture, the adsorption of CH_4 and H_2 is noteworthy, reflecting their potential significance in energy storage, for example, for future automotive applications [37].

The recovery of C2 hydrocarbons, especially C_2H_4, from natural gas is economically feasible and meaningful. Ethylene is a crucial chemical for the production of polymers, primarily polyethylene, polyester, polystyrene, polyvinyl chloride, and other organic chemicals [38].

Considering the above issues, we investigated the possibility of using activated carbon produced from fern leaves to separate gas mixtures such as CO_2/N_2, CO_2/H_2, CO_2/CH_4, and C_2H_4/CH_4. Initially, we conducted measurements of the adsorption isotherms for pure CO_2, N_2, CH_4, H_2, and C2H4 onto activated carbons produced from fern leaves activated by H_3PO_4 and carbonized in three different temperatures (700, 800, or 900 °C). The Toth model [26] was utilized as input to forecast adsorption equilibria in binary mixtures, employing the ideal adsorption solution theory (IAST) [11,39] To the best of our knowledge, fern leaves have not been reported in the literature as AC raw material in sorption applications for such a wide range of gaseous substances, including greenhouse gases or clean energy transition fuel. This study presents an innovative approach to producing activated carbons (ACs) from fern leaves, offering a sustainable and readily available alternative to traditional materials. The process involves activation with phosphoric acid (H_3PO_4) followed by thermal conversion at temperatures ranging from 700 to 900 °C. This method yields ACs with potentially exceptional adsorption properties characterized by increased specific surface area and pore volume, which enhance their capability to capture a variety of gases under high-pressure conditions, including CO_2, CH_4, H_2, N_2, and C_2H_4. Motivated by the need to address environmental challenges and advance clean energy technologies, this research investigates the application of fern-derived ACs in gas separation processes. Initial experiments focused on measuring adsorption isotherms for pure CO_2, N_2, CH_4, H_2, and C_2H_4 on ACs produced from fern leaves activated by H_3PO_4 and carbonized at temperatures of 700, 800, or 900 °C. The Toth model was employed to predict adsorption equilibria in binary mixtures, utilizing the ideal adsorption solution theory (IAST). Significantly, fern leaves have not previously been utilized as a raw material for ACs in such a broad spectrum of gas sorption applications, including greenhouse gases and clean energy transition fuels. This novel utilization underscores the potential of waste biomass, such as fern leaves, as a cost-effective and efficient adsorbent in mitigating global warming effects and facilitating the transition towards renewable energy sources.

In summary, this research contributes to the development of sustainable adsorption technologies by exploring the innovative use of fern-derived ACs. By demonstrating their efficacy in gas separation and highlighting their environmental benefits, this study sets a precedent for utilizing abundant natural resources in advancing gas sorption science and promoting global sustainability efforts.

2. Materials and methods

2.1. Synthesis of porous carbons

Impregnation with phosphoric acid and pyrolysis treatment was applied to prepare the carbon precursor derived from fern leaves. In detail, the procedure of preparation was as follows: the material was collected and then dried at 120 °C for 12 h, and the material was then ground into a powder. Then, chemical activation was performed with 70 % H_3PO_4 solution in a ratio of 1:1 for 3 h at room temperature. After the reaction, the brownish product was transferred to a stainless-steel boat, and thermal treated into a horizontal tube furnace with stainless steel reactor (Carbolite ®), under a constant nitrogen flow (15L/h), followed by being heated at a ramp of 5 °C/min until different temperatures, 700, 800, or 900 °C for 1 h, and then cooling in a CO_2 atmosphere with a flow of 15 L/h, to produce the samples FERN700, FERN800 and FERN900, respectively. Then, every sample was washed thoroughly with warm distilled water until the filtrate had a constant pH value and then they were dried at 100 °C for more than 12 h (Fig. 1).

2.2. Physicochemical characterization

The textural parameters of specific surface area (S_{BET}), pore volumes (V_t and V_{micro}) and pore size distribution were evaluated through the experimental data of nitrogen adsorption isotherms at −196 °C and CO_2 at 0 °C. a, as appropriate. These data were obtained in a semi-automatic Autosorb IQ2 sortometer equipment, and the data were processed in the ASIQWin software using the BET, and the density functional theory (DFT) by the QSDFT model.

To analyze the micromorphological structure of cuticular waxes, a fresh leaf segment (1 cm^2) was placed with the adaxial surface facing upwards onto a sample holder. After drying at room temperature and the usual gold–palladium sputtering (Denton Vacuum Desk II sputter coater), photomicrographs were taken with a SEM (Jeol JSM-5310LV), at 45° tilt. Images were acquired by ORION software and processed with Adobe Photoshop CS5 v. 12.0. Micromorphological wax classification was followed by Barthlott et al [40].

The X-ray fluorescence energy dispersion spectrophotometer (EDXRF) of Epsilon 3 type from PANalytical B.V was used to determine the content of other elements in derived activated carbons. Moreover, the yield content in the obtained activated carbons was determined in accordance with PN-84 / C-97555/08 [41]. The principle of this method is complete combustion of organic substances that are contained in the material and calcination to a constant mass at a temperature of 814.5 °C ± 15 °C. Then the arithmetic average of three measurements between which the difference does not exceed 5 % is calculated. The yield content (YC) in the obtained activated carbons was determined in accordance with PN-84/C-97555/08 [24]. The method is based on the complete combustion of organic substances that are contained in the material and calcination to a constant mass at a temperature of 1088 ± 288 K. The average of three measurements between which the difference does not exceed 5 % of the arithmetic average is taken as the final result. The yield content in the activated carbon sample was determined according to equation (1):

$$Yc = \frac{W_3 x W_1}{W_2 x W_1} x100\% \quad (1)$$

where: W_1- weight of roasted container [g]; W_2- weight of container with activated carbon [g]; W_3- weight of the container with yield [g].

A PANalytical Empyrean diffractometer equipped with a sample of CuKα was used to analyze the phase composition of active carbons. The prepared diffractograms were analyzed and compared to the location and intensity of the reflections on the obtained diffractograms with the standard diffractograms contained in the ICDD PDF4 + 2015 database based on the X'Pert HighScore program.

For the Raman spectroscopy tests, the samples were taken in an XPlora Raman Horiba spectrometer that is coupled to an Olympus BX41 Microscope. The team has three lasers: the first is an air-cooled diode laser, with a power of 90 mW (for 785 nm); the second laser is an air-cooled diode of 4 mW power (for 638 nm); and the third laser is a mW power doped ruby crystal (for 532 nm). The operating characteristics of the microscope for the samples were as follows: 100 % filter, 532 laser, 600 grating and an aperture of 5x_0.80.

Mössbauer spectra were obtained in a spectrometer equipped with twelve channels with constant acceleration and geometry of transmission. A source of ^{57}Co was used in a matrix of Rh of 50 me normal. All isomeric shifts were related to a standard at 25 °C. Lorentzian lines of the same width were used for each component of the spectra. All the spectra were fitted, and the hyperfine parameter distributions were obtained to quantify the different phases of the iron oxides. The spectra were obtained at room temperature and folded to minimize geometric effects, being evaluated using a commercial computer fitting program named Recoil.

The hydrophobic factor of the samples was evaluated through the immersion calorimetry technique, for this, the immersion enthalpies, ΔH_{Imm}, in benzene and in water were evaluated. The experimental data were obtained in a passive diathermic calorimeter of home-made

Fig. 1. Schematic preparation procedure of activated carbons.

construction. In detail, approximately 100 mg of the sample was weighed into a glass cell, which has a fragile peak. The calorimeter consists of a heat reservoir that contains a thermopile-type sensor system, adapted to the geometry of the calorimetric cell, which contains 8 mL of the wetting liquid. By coupling the parts of the calorimeter in the heat reservoir, the data is collected in a multimeter coupled to a computerized system, once the thermal equilibrium is reached, which is assumed when there is a baseline, the glass cell is immersed, after breaking the peak, with the bottom of the calorimetric cell, now the wetting liquid is entered, while a change in the signal related to the heat involved in the interaction between the solid and the liquid has been registered. Later, when the signal returns to the baseline, an electrical calibration is carried out to know the electrical work and constant of the calorimeter to calculate ΔH_{Imm} from the signal obtained in the immersion step.

2.3. High-pressure gas adsorption

The adsorption of gases such as carbon dioxide, nitrogen, hydrogen, methane, and ethylene under pressure conditions higher than 1 bar was investigated by the volumetric method using the IMI Hiden Isochema apparatus. All gas adsorption measurements were performed at room temperature. The preparation consisted of placing ~2 cm^3 of the sample into the reaction tank and closing it. To check the tightness of the helium-flushed system. The next stage was the degassing of the sample at the temperature of 250 °C for 12 h. Then, the measurements of the isotherms of adsorption were performed.

2.3.1. Adsorption isotherms

To describe the adsorption equilibrium were used different models: Langmuir, Freundlich, Toth, Sips, Fritz – Schlunder, Radke-Prausniz, UNILAN. In order to evaluate the best fittings of isotherm models to the experimental data has been applied the least-squares method (LSM), which is most commonly used as error functions. This method is described by equation (2):

$$LSM = \sum_{i=1}^{Np} \left(q_{e,o} - q_{e,z}\right)^2 \tag{2}$$

where: $q_{e,o}$- theoretical adsorption capacity calculated from the model, $q_{e,z}$ – adsorption capacity determined experimentally, Np – total number of measurements.

2.3.1.1. Langumir isotherm model. The Langmuir equation describes an adsorption model leading to the formation of a monomolecular layer on the surface of the adsorbent. It is assumed that there are a certain number of energetically homogeneous centers, sites of adsorption, on the surface, each of which can adsorb only one molecule of the adsorbate [42,43]. Moreover, it is assumed that there are no interactions between the molecules adsorbed on the surface of the solid body. The Langmuir isotherm equation is given by the equation (3):

$$q = \frac{q_{mL} \bullet b_L \bullet p}{1 + b_L \bullet p} \left[\frac{mmol}{g}\right] \tag{3}$$

where: q_{mL} – the maximum adsorption capacity [mmol/g], b_L – the Langmuir constant [bar^{-1}], p – pressure [bar], q – the adsorbed quantity under p pressure [mmol/g].

2.3.1.2. Freundlich isotherm model. The Freundlich equation is the first and best-known empirical equation used to describe heterogeneous systems that can be characterized by the heterogeneity factor 1/n. This equation well describes the reversible adsorption from dilute solutions. In Freundlich's theory, the number of adsorbed molecules with complete coverage of the adsorbent surface cannot exceed the number of active sites [44]. Freundlich equation is expressed by an equation (4):

$$q = k_F \hat{A} \cdot p^{nF} [mmol/g] \tag{4}$$

where: k_F – the Freundlich constant [mmol/g], n_F – the heterogeneity factor

2.3.1.3. Toth isotherm model. The Toth isotherm model is another empirical equation developed to improve isotherm fitting between experimental data and the equilibrium data's predicted value. The Toth isotherm model is useful in describing heterogeneous adsorption systems, which satisfies both low and high-end boundaries of the concentration [45,46]. Toth equation can be described as follows (5):

$$q = \frac{q_{mT} b_T p}{\left(1 + (b_T p)^{nT}\right)^{\frac{1}{nT}}} [mmol/g] \tag{5}$$

where: q_{mT} – the maximum adsorption capacity [mmol/g], b_T – the Toth constant [bar^{-1}], n_T – the heterogeneity factor

2.3.1.4. Sips isotherm model. The Sips isotherm model is a combination of the Langmuir and Freundlich isotherms. It is useful for adsorption on heterogeneous surfaces. It is reduced to the Freundlich model at low adsorbate concentrations, and at high adsorbate concentrations, it is similar to the Langmuir model [47,48]. The Sips isotherm is expressed by an equation (6):

$$q = \frac{q_{mS} \hat{A} \cdot b_S p^{ns}}{1 + b_S \bullet p^{ns}} [mmol/g] \tag{6}$$

where: q_{mS} – the maximum adsorption capacity [mmol/g], b_S – the Sips constant [bar^{-1}], n_S – the heterogeneity factor

2.3.1.5. Fritz – Schlunder isotherm model. Fritz and Schlunder derived an empirical equation that can fit a wide range of experimental results due to many coefficients in the isotherm [49]. Fritz – Schlunder is given by (7):

$$q = \frac{q_{mFS} b_{FS} p}{1 + q_{mFS} p n_{FS}} [mmol/g] \tag{7}$$

where: q_{mFS} – the maximum adsorption capacity [mmol/g], b_{FS} – the Fritz- Schlunder constant [bar^{-1}], n_{FS} – the Fritz – Schlunder model exponent

2.3.1.6. Radke – Prausnitz isotherm model. The Radke-Prausnitz model has several important properties that make it the preferred choice for most adsorption systems with low adsorbate concentrations. At a low adsorbate concentration, the isotherm model reduces to a linear isotherm. In contrast, at a high adsorbate concentration, it approaches the Freundlich isotherm, and when $n_{RP} = 0$, it becomes a Langmuir isotherm. Another essential feature of this isotherm is that it provides a good fit over a wide range of adsorbate concentrations. Radke – Prausnitz equation is expressed as (8):

$$q = \frac{q_{mRP} \bullet b_{RP} \hat{A} \cdot p}{(1 + b_{RP} \hat{A} \cdot p)^{n_{RP}}} [mmol/g] \tag{8}$$

where: q_{mRP} – the maximum adsorption capacity [mmol/g], b_{RP} – the Radke – Prausnitz constant [bar^{-1}], n_{RP} – Radke – Prausnitz model exponent

3. Results and discussion

3.1. Textural characterization

The textural characteristics of the different FERN carbonaceous materials were determined by sorption of N_2 at 77 K. N_2

adsorption–desorption isotherms for FERN carbonaceous materials are shown in Fig. 2. As can be seen the materials prepared using phosphoric acid as activating agent are microporous with a moderate development of mesoporosity; described by the small hysteresis loop, and pore size distribution up to 30 nm, evaluated by DFT model.

The isotherms obtained from N_2 adsorption can be classified as type I (a) for FERN 700, and type IV for FERN 800 and FERN 900, according to the recent IUPAC classification [50,51]. Type I isotherm is associated with microporous structures and a type IV isotherm indicates a mixture of microporous and mesoporous materials. The initial part of the isotherms is of type I with significant uptake at low relative pressures, which corresponds to adsorption in micropores. At intermediate and high relative pressures, the isotherms are of type IV with a hysteresis loop of type H4 associated with monolayer–multilayer adsorption followed by capillary condensation in narrow slit-like pores [9]. Nitrogen uptake increases with increasing activation temperature indicating the gradual development of the porous structure. With the increase in temperature of carbonization, it is found that the hysteresis loop gradually widens indicating that the activated carbons get populated with mesopores. For all temperatures, a plateau is not apparently reached rather adsorption occurs over the entire pressure interval indicating the presence of a wide range of pore diameters. It can be stated that the activated carbons obtained have both micropores and mesopores, which is confirmed by the pore distribution presented in Fig. 3. Similar results were reported by other researchers [52–54].

Fig. 3**(a)** shows the pore size distributions (PSD) of the carbonaceous materials obtained from the experimental data of adsorption of N_2 at 77 K and Fig. 3**(b)** corresponds to PSD from the experimental data of CO_2 at 273 K. Nitrogen experimental data were fitted to two microscopic models: Non-Local Density Functional Theory (NLDFT) and Quenched Solid Density Functional Theory (QSDFT) and the different geometries: Slit, cylindrical and combined [55], among these models, the one with the best fit was the QSDFT of combined geometry (Slit-cylinder). A better fit to the QSDFT in carbonaceous materials describes a rough surface of solids geometrically and chemically heterogeneous [55,56]. When comparing the PSD calculated for the two adsorbates (N_2 and CO_2) it is observed that the samples have a greater contribution of microporosity with pore width less than 2 nm, however moderate volumes of mesopores between 2.0–15.0 are observed nm, being more evident for the FERN800 and FERN900 samples.

Table 1 summarizes the textural characteristics of carbonaceous materials, from N_2 adsorption data were calculated the BET area (S_{BET}) for the FERN solids, this parameter is between 357–438 m^2/g, also were calculated the micropore volumes ($V_{o(N2)}$), for these are between 0.212–0.300 cm^3/g, respectively. Differences in features found among

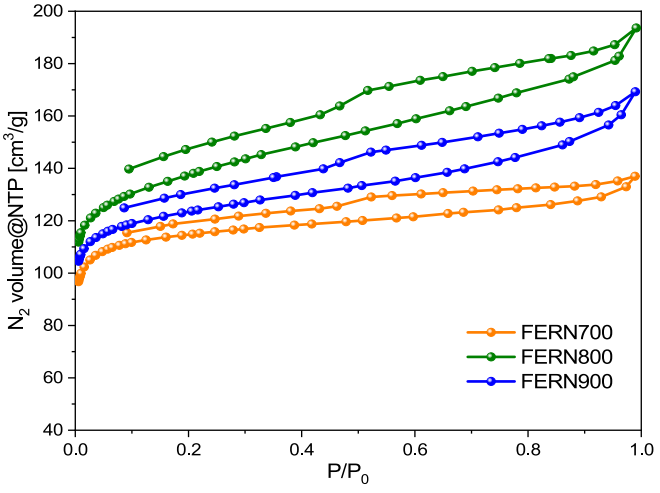

Fig. 2. N_2 adsorption–desorption isotherm from FERN materials at 77 K.

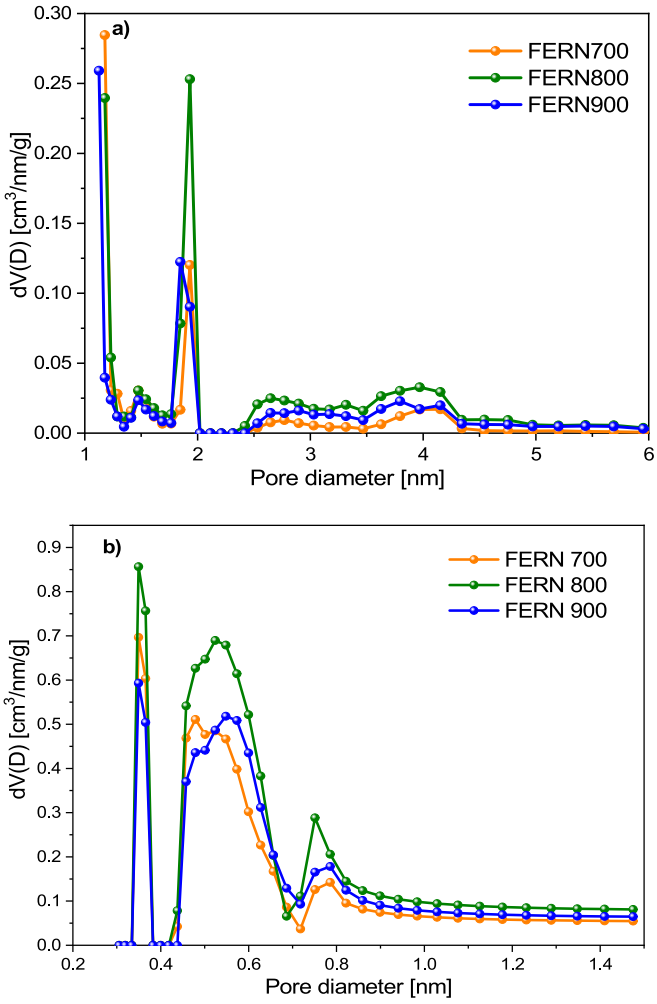

Fig. 3. PSD of FERN materials evaluated from (a) N_2 data at 77 K by slit-cylinder QSDFT model and (b) CO_2 data at 273 K by NLDFT model.

carbonaceous materials show that the activating agents used have a different effect on the properties of activated carbons depending on the temperature used. Additionally, Table 1 shows the volume of narrow micropores (V_n) those with diameters less than 0.8 nm obtained from the CO_2 adsorption isotherm at 273 K, as can be seen for all the samples $V_{0\,(CO2)} > V_n$, which reflects the absence of kinetic restrictions for N_2 to access the narrow microporosity. However, it can be observed that for the FERN 700 and FERN 900 samples the content of V_n value in $V_{0(CO2)}$ corresponds to 75.6 and 74.6 %, while for FERN 800, it is around 73.4 %, indicating a little bit less narrow pore size distribution located at diameters lower than 0.8 nm for this sample.

3.2. Morphological and chemical characterization

3.2.1. Scanning electronic microscopy (SEM)

Fig. 4 shows the micrograph of the impregnated solids submitted

Table 1
Textural properties evaluated from N_2 adsorption data at 77 K, and CO_2 adsorption capacity at 273 K.

Sample	S_{BET} [m^2/g]	V_T [cm^3/g]	$V_{0(N2)}$ ≤ 2 nm [cm^3/g]	$V_{0(CO2)}$ ≤ 1.47 nm [cm^3/g]	V_n ≤ 0.8 nm [cm^3/g]
FERN 700	357	0.212	0.165	0.164	0.124
FERN 800	438	0.300	0.236	0.193	0.176
FERN 900	387	0.263	0.180	0.174	0.132

under targeted pyrolysis temperature, the morphological characteristics of activated carbons are apparently similar between them, however with respect to the starting material the destruction of the surface is observed as a result of the thermal and chemical degradation process in the first phase of impregnation due to initial depolymerization effect of the activating agent H_3PO_4, it revealed that the structure and surface was partially attacked under the impregnation and pyrolysis conditions, but mainly smooth surfaces are maintained.

3.2.2. Compositional and proximal analysis

Chemical composition evaluated by X-Ray Fluorescence (XRF), summarized in Table 2 revealed the presence of different heteroatoms, among these: elemental silicon (Si) is present in these solids, considering that silicon is the second most abundant element in the earth's crust, due to this it is very common to find different silicon compounds as part of plants. Silicon also provides mechanical and physical protection to plants and improves their UV tolerance. The presence of other trace elements has also been reported such as: P, which is an essential nutrient that is part of several structural compounds in plants and acts as a catalyst for biochemical reactions, especially due to its role in capturing and converting the sun's energy into useful plant compounds. Part of the reported phosphorus can also come from impregnation with the activating agent, H_3PO_4. Furthermore, K is a macronutrient that enhances the ability of the plant to defend to biological stress, intervenes in the nitrogen fixation process, it intervenes in several enzymatic processes as well as in the production of macromolecules essential for the operation of the plant. Ca, it plays an important role to produce plant tissues, also participates in certain enzymatic mechanisms. Fe is a micronutrient present in most living organisms, specifically in plants it can intervene in processes such as photosynthesis, and enzymatic processes in which redox reactions occur, where iron acts as a cofactor for its ability to gain and lose electrons. The chloride ion is an essential micronutrient in plants and participates in various metabolic processes such as photosynthesis, resistance and tolerance to diseases, osmotic and stomatal regulation. Cu is a micronutrient that acts in several enzymatic processes, including photosynthesis, lignin synthesis, protein and carbohydrate metabolism, and plant respiration.

Table 2
Proximal and compositional analysis, the latter evaluated by XRF.

Sample parameter	FERN 700	FERN 800	FERN 900
Moisture [%]	6.91	8.92	15.8
Volatile Matter [%]	10.1	27.4	13.4
Ash [%]	15.1	22.8	47.0
Fixed Carbon [%]	67.9	41.0	23.8
C Yield content [%]	39.8	28.1	32.7
Si [%]	1.57	1.03	0.82
P [%]	1.70	4.01	9.61
K [%]	0.67	8.79	5.08
Ca [%]	7.91	2.91	2.22
Fe [%]	5.42	2.82	11.3
Total XRF [%]	18.55	20.00	29.34

The presence of each of these heteroatoms suggests the enrichment of the inorganic phase due to the condensation of the inorganic components of the ferns in the pyrolysis process, and slow decomposition of the organic polymers, therefore the smoother surface of the activated carbon due to low and homogeneous decomposition. The presence of these inorganic components can form active sites of interaction for some of the molecules selected for study.

Table 2 also includes the proximal analysis that was made for FERN materials, in general, it is observed that carbonaceous materials have a volatile matter content that ranges between 10.1 and 27.4 %, and fixed carbon percentages ranging between 23.8 and 67.9 %, although this percentage for FERN800 is low, with respect to other carbonaceous materials, the effect of the ash content on the preservation of the carbonaceous phase during the pyrolysis process is also evident.

The activated carbon yield is defined as the ratio of the weight of activated carbon after activation, washing and drying to the weight of the dried fern leaves residue. As can be seen from Table 2, when the

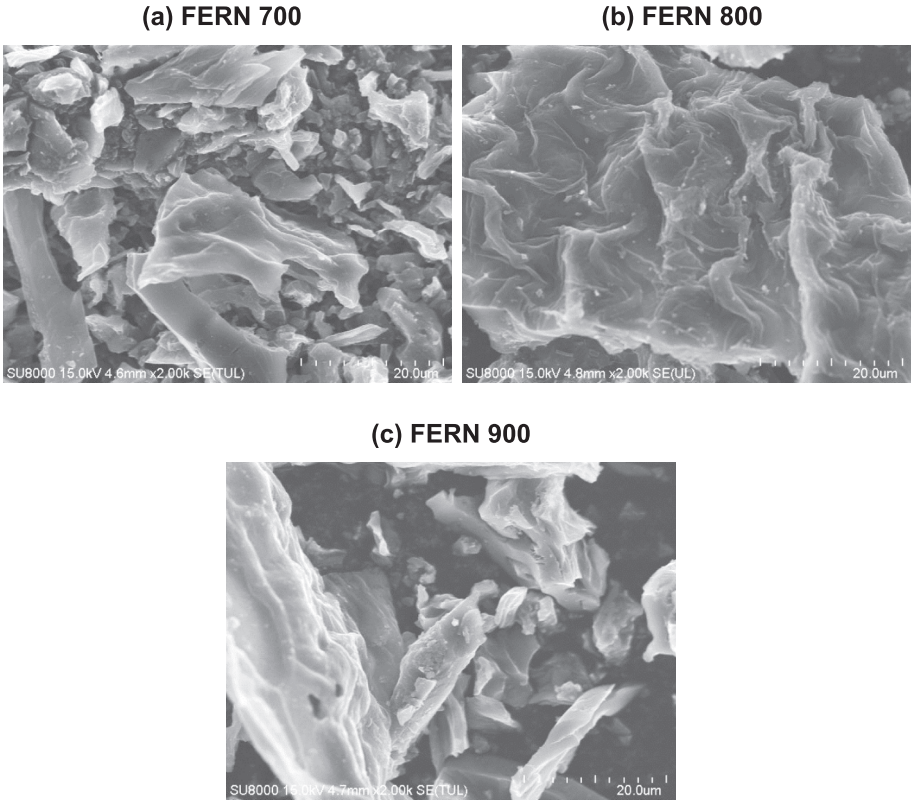

Fig. 4. SEM micrograph of the materials **(a)** FERN700, **(b)** FERN800 and **(c)** FERN900.

activation temperature increased from 700 to 900 °C, the activated carbon yield decreased from 39.8 to 28.1 %. Along with the increase in carbonization temperature, there was a loss of mass, which was related to the loss of volatile materials. The use of phosphoric acid in the activation process promotes depolymerization, dehydration and redistribution of the biopolymer components, thus increasing the final yield of activated carbon [57].

3.2.3. X-ray diffraction analysis

The results of the X-ray diffraction pattern in Fig. 5 show broad asymmetric diffraction peaks that are located at $2\theta = 24°$, indicating the formation of a turbostatic random carbon structure. A second peak at $2\theta = 43°$ also appeared in the activated carbon patterns; this can be indexed to diffraction on (1 0 0) graphite planes (JCPDS sheet no. 41-1487), showing that the activated carbons made of common fern have a low degree of graphitization [58]. The XRD study of activated carbons showed a high intensity of the background, indicating that we are working with a disordered material, i.e., amorphous carbon. All three samples show the presence of an amorphous phase because the graphite reflex corresponding to the 002 level is superimposed on an intense background with an angle of 15-30°. The highest value of intensity is observed for FERN 800 activated carbon. Zięzio et al. [59] obtained similar results.

3.2.4. Raman spectroscopy

Fig. 6 shows the Raman spectra of the FERN materials, Raman spectroscopy can provide key information about material structure. Three major regions are detected at frequencies located at 1311 cm^{-1}, D band, correlated with the disorder-induced band often seen in defective graphenic materials, also depends on the number of the sp^3 carbon atoms; 1599 cm^{-1}, G band, corresponds to the C–C stretching mode, and 1760 cm^{-1}, 2D band that supported the formation of the 2D graphenic crystallites [60,61]. The intensity ratio of the D band to G band (I_D/I_G) indicates the degree of graphitization and the level of the disorder and the number and size of the sp^2 cluster, while that (I_{2D}/I_G) between the 2D band and the G band was utilized to estimate the layer number of the graphene nanosheets. The I_D/I_G and I_{2D}/I_G are summarized in Table 3, values are 0.535–1.717 and 0.1848–1.766, respectively, which indicate the growth of few-layered graphene-based nanosheets.

3.2.5. Mössbauer spectroscopy

The Mössbauer spectra of the samples are shown in Fig. 7**.** All spectra showed a central doublet with shoulders on both sides and two wide lines in the negative and positive velocities range. In addition, the valleys between these peaks do not reach the baseline and because of this

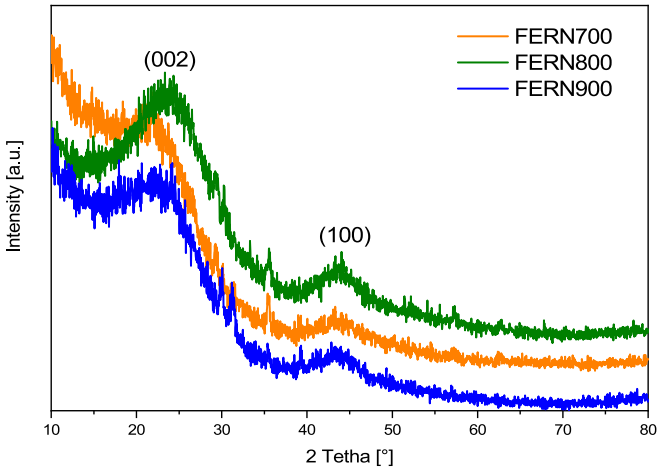

Fig. 5. XRD diffractogram and of FERN materials.

the background seems curved. This is a characteristic of systems with magnetic relaxation due to the small crystal sizes. All spectra were fitted with two magnetically blocked sextuplets, two relaxing sextuplets and a doublet. The two magnetically blocked and partially resolved sextuplets (red curves in Fig. 6) can be assigned to the Fe^{3+} ions located in tetrahedral sites (A sites) and to the $Fe^{2.5+}$ ions in the octahedral sites (B sites) of magnetite (Fe_3O_4). The values of hyperfine magnetic fields are slightly decreased compared to typical values of bulk magnetite. This can be attributed to the existence of "collective magnetic excitations" due to the small size of the crystals. The two relaxing sextuplets (black curves in Fig. 7) were fitted using the model of two-state relaxation proposed by Blume and Tjon [62] and also have typical hyperfine parameters of the A and B sites of magnetite, but now, the hyperne magnetic fields are even smaller than those magnetically blocked due to magnetic relaxation effects.

These results indicate a broad distribution of magnetite particle sizes, so that the fraction related to the larger particle sizes produces magnetically blocked signals but with reduced fields due to fluctuations of the magnetization vector around the easy magnetization directions, while the fraction of smaller particle sizes produces magnetically relaxing signals. Also, when magnetite particles have sizes small enough to show superparamagnetic relaxation and the signal collapses to a singlet, it is reasonable to rule out that the central doublet (black line in Fig. 6) corresponds to this species. Besides, it does not seem probable that this doublet, with a typical isomer shift of Fe^{3+}, may correspond to paramagnetic Fe^{3+} ions exchanged or widespread within the activated carbon, since these kinds of supports do not exhibit these characteristics. The doublet is assigned to superparamagnetic hematite (α-Fe_2O_3) for these reason. From the Mössbauer it is possible supposed that the magnetite particles are formed mainly inside the support pores, during heating, from impregnated iron nitrate. It is believed that hematite is produced first since there is no Fe^{2+} species from the starting materials. After some time, carbon monoxide is produced from activated carbon and is able to reduce some Fe^{3+} to Fe^{2+} species to produce magnetite. However, as the reduction should begin on the surface, it is probable that some hematite remains as a core in the particle because of the inaccessibility of carbon monoxide. Therefore, the resulting particles are made of a hematite core surrounded by magnetite.

Only hematite could be identified in three different magnetic regimes: magnetically locked, in collective magnetic excitation and in a magnetic relaxation state. The first fraction corresponds to the larger particles while the second one has a size large enough to show a not relaxing behavior, but their magnetic hyperfine field was decreased by the collective magnetic excitation phenomena. Finally, the third corresponds to very small particles, which are in a state of magnetic relaxation. Considering the previous description related to the richest iron catalysts, one can suppose that as the iron load gets very low, the occlusion of carbon pores is negligible. Therefore, diffusion restrictions for the iron richest samples are also negligible. As a result, the carbon monoxide formed by the partial combustion of the support is rapidly eliminated, so that the partial reduction of hematite to magnetite does not occur. Table 4 shows the total percentages of both magnetite and hematite contained in the activated carbons prepared. It can be noted that magnetite is the major component and that there is no significant difference between the percentages of the phases for the different catalysts within experimental error.

3.2.6. Immersion calorimetry

Carbonaceous materials were enthalpically characterized using the calorimetric technique. Table 5 shows the immersion enthalpies of the FERN carbons in water and in benzene, which allows the establishment of the hydrophobic and hydrophilic character of the solids. Fig. 8**(a)** shows an increase in the enthalpy of immersion in benzene with the increase in the BET area of carbon materials, due to the proportionality between the immersion enthalpy and the surface area accessible to the immersion liquid. Moreover, Fig. 8**(b)** shows the correlation between

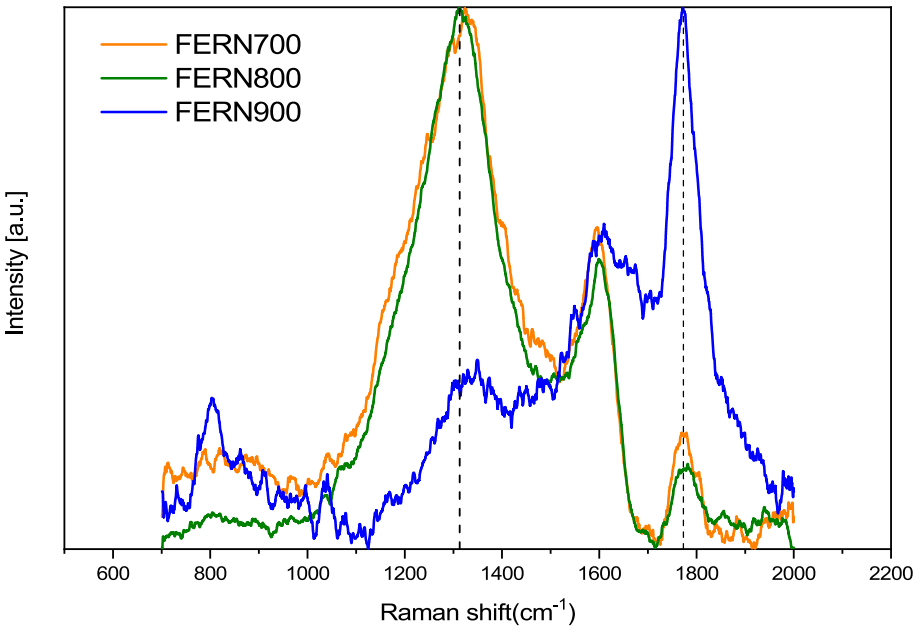

Fig. 6. Raman spectra of FERN materials.

Table 3
Raman parameters obtained by FERN materials.

Sample	I_D/I_G	I_{2D}/I_G
FERN700	1.717	0.1848
FERN800	1.824	0.249
FERN900	0.535	1.766

the ash content, total XRF versus the moisture content, considering that these inorganic groups can function as groups of interaction between the water molecules in the environment and with the fountain liquid in the calorimetric cell. These correlations turn out to be proportional, being very evident in the determination of inorganic sites. While the correlation between the hydrophilic factor and the moisture content, as presented in Fig. 8**(c),** is a little more dispersed, considering that the surface of an activated carbon is composed of basal units. They strictly correspond to the basal planes with a high electron density and a series of polar sites at the edges of the carbon layers frequently composed of oxygen, forming various functional groups with different acid-base properties. Therefore, all the interactions that are established between the surface of FERN carbons and a polar molecule such as water are determined by the content of total surface groups present in the carbons.

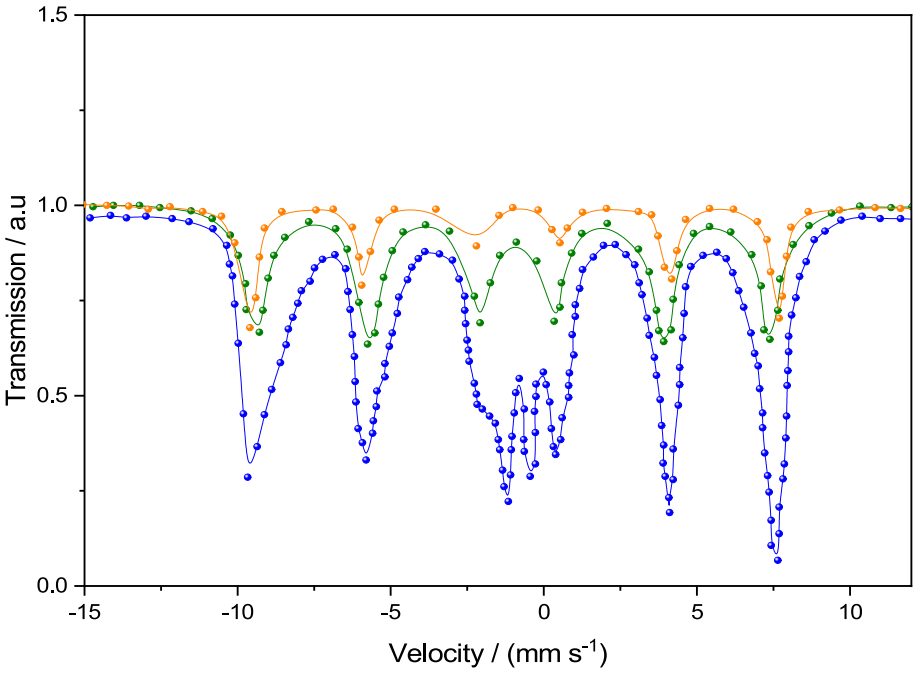

Fig. 7. Mössbauer spectra for FERN materials, FERN700 is the orange line, FERN800 is the green line, and FERN900 is the blue line. (For interpretation of the references to colour in this figure legend, the reader is referred to the web version of this article.)

Table 4
Amounts of magnetite (Fe_3O_4) and of supermagnetic hematite ($\alpha - Fe_2O_3$ (sp)) in the catalysts obtained from Mössbauer spectra of FERN700, FERN800 and FERN900 samples (activated carbon from Fern Leaves). The numbers represent the iron amount (wt.%) found in the activated carbon.

Sample	Fe_2O_4 [%]	α-Fe_2O_3 (sp) [%]
FERN 700	88 ± 11	12 ± 1
FERN 800	80 ± 9	10 ± 1
FERN 900	75 ± 7	15 ± 1

Table 5
Immersion enthalpies in water and benzene of FERN materials, and the Hydrophobic Factor.

Sample	ΔH_{Imm} H_2O [J/g]	ΔH_{Imm} C_6H_6 [J/g]	ΔH_{Imm} C_6H_6/ ΔH_{Imm} H_2O Hydrophobic Factor	ΔH_{Imm} H_2O / $\Delta H_{Imm}C_6H_6$ Hydrophilic Factor
FERN700	−11.2	−46.3	4.13	0.242
FERN800	−24.4	−54.8	2.24	0.446
FERN900	−28.0	−60.9	2.18	0.459

3.3. High pressure adsorption of ethene, hydrogen, methane, nitrogen and carbon dioxide

The comprehension of the adsorption characteristics of gases at elevated pressures holds significant importance owing to its extensive consequences across diverse disciplines such as industrial operations, energy storage, and materials research. The acquisition of high-pressure adsorption data is of utmost importance as it offers valuable insights into the interactions between gases and adsorbents. This section presents the high-pressure adsorption results at 298 K of ethene, hydrogen, methane, nitrogen, and carbon dioxide on the prepared carbonaceous materials. These investigations aim to elucidate the unique behaviors shown by these gases and their potential implications for practical applications. Figs. 9 and 10 illustrate the adsorption capacity of ACs within a pressure range between 0 to 45 bar for each tested gas.

FERN800 stands out for its remarkable gas uptake capacities among all the samples. FERN800 exhibited the greatest of C_2H_4, H_2, CH_4, and CO_2 uptake values of 3.36, 1.19, 3.14, and 4.21 mmol/g at a pressure of 45 bar, respectively. The N_2 uptake of FERN 800 was evaluated to be 2.04 mmol/g. In contrast, FERN700 and FERN900 demonstrated comparatively reduced performance in terms of C_2H_4, H_2, CH_4, and CO_2 adsorption at the same pressure, reaching 2.91, 1.19, 2.59, 3.79 mmol/g and 3.15, 0.99, 2.83, 3.74 mmol/g. The observed differences underscore the impact of activation temperature on the adsorption efficiency, which is reported by many of our previous studies [63,64]. Additional investigation and examination may be required in order to comprehend the ramifications of the activation temperature on the textural characteristics and its relationship with sorption performance.

Furthermore, the augmentation of pressure has been seen to significantly enhance the adsorption of gases onto activated carbon solid surface, particularly in instances of physical adsorption. This observation aligns with Le Chatelier's principle, a notion in chemical equilibrium that posits an increase in pressure would promote the side of the reaction during the adsorption phenomenon [65]. As the pressure is raised, there is an associated increase in the concentration of molecules inside the gaseous phase, leading to the more efficient accumulation of them on the surface of ACs derived from fern leaves [66]. Table 6 shows comparison of C_2H_4, H_2, CH_4, and CO_2 uptake on adsorbents at 45 bar and 25.

3.3.1. Influence of textural properties on adsorption performance

Fig. 11 show the correlation of the total amount of this gas adsorbed in each of the carbonaceous materials with the textural parameters, at atmospheric pressure that can provide insights into gas selectivity and affinity. This includes BET surface area (Fig. 11**(a)**), total pore volume (Fig. 11**(b)**), micropore volume (Fig. 11**(c)**) and narrow micropore volume (Fig. 11**(d)**. The varying R^2 values with small differences for different textural parameters and the adsorption of ethene (R^2: 0.99–0.88) and methane (R^2: 0.99–0.90) on ACs suggest a complex adsorption mechanism influenced by a combination of factors. The intricate nature of this phenomenon may arise from a multitude of variables, including the size and shape of the gas molecules, their polarity, and the distinct chemical reactions taking place at the adsorption sites inside the material. On the other hand, hydrogen ($R^2 = 0.94$) and nitrogen ($R^2 = 0.91$) exhibited high R^2 values for total pore volume, which suggests that gas adsorption is influenced by the overall pore structure. This could indicate that gases are adsorbed in larger pores or that pore volume affects gas accessibility and diffusion within the material. Finally, based on the highest R^2 (0.97–0.99) for carbon dioxide, the adsorption mechanism is directly related to the interaction of this adsorbate with the walls of the pores smaller than 2 nm, especially narrow micropores. Therefore, it could be concluded that the CO_2 adsorption mechanism depends crucially on the pore size distribution.

3.3.2. Influence of chemical properties on adsorption performance

During our rigorous investigation into the adsorption behavior of gases on ACs, several notable correlations between chemical parameters and adsorption capacity can be seen in Fig. 12, applying the same procedure as previously. Notably, these correlations shed light on the intricate interplay of surface characteristics and gas affinity. The hydrophilic and hydrophilic factors displayed a positive correlation with H_2 (R^2: 0.94–0.95) and N_2 (R^2: 0.97–0.98), likely due to the polar and nonpolar nature of gases. In the case of moisture content, it exhibited the highest positive correlation with C_2H_4 (R^2: 0.89) and CH_4 uptake (R^2: 0.93), underscoring the role of ACs surface moisture in gas capture. Finally, XRF analysis, reflecting the inorganic composition, showed high R^2 values for CO_2 (R^2: 0.99). The presence of certain inorganic components in the activated carbon could impact CO_2 adsorption acted as potential catalysts or modifiers. These correlations offer valuable insights into the nuanced relationships between chemical parameters and gas adsorption on activated carbons, illuminating the complex interplay of surface properties and gas-specific affinities.

3.3.3. Modeling of the H_2 adsorption process

Adsorption models are very useful because they predict the behavior of the adsorption equilibrium over a wide range of temperatures and pressures. Typically, models with two or three parameters are used to describe isotherms on activated carbon [72]. Various mathematical equations are used to describe the adsorption isotherms. These equations determine the total amount of adsorbed gas q [mmol/g] depending on the pressure p [bar]. To describe the experimental adsorption isotherms of gases such as CO_2, H_2, CH_4, C_2H_4 and N_2 at the temperature of 25 °C, equations with two Langmuir and Freundlich parameters and equations of adsorption isotherms with three parameters Sips, Toth, Unilan, Radke-Prausniz and Fritz-Schlunder were used. The least squares method (LSM), described by the equation [73]:

$$LSM = \sum_{i=1}^{n} \left(q_{e,o} - q_{e,z}\right)^2 \quad (9)$$

where:

$q_{e,o}$ – theoretical adsorption on the sorbent surface calculated based on the model
$q_{e,z}$ – adsorption on the sorbent surface determined experimentally

Toth's equation was found to give the highest accuracy of fit to all experimental data which is a commonly used isotherm model in adsorption studies, and it's known for its versatility in fitting experimental data accurately, especially for complex adsorption behavior. In

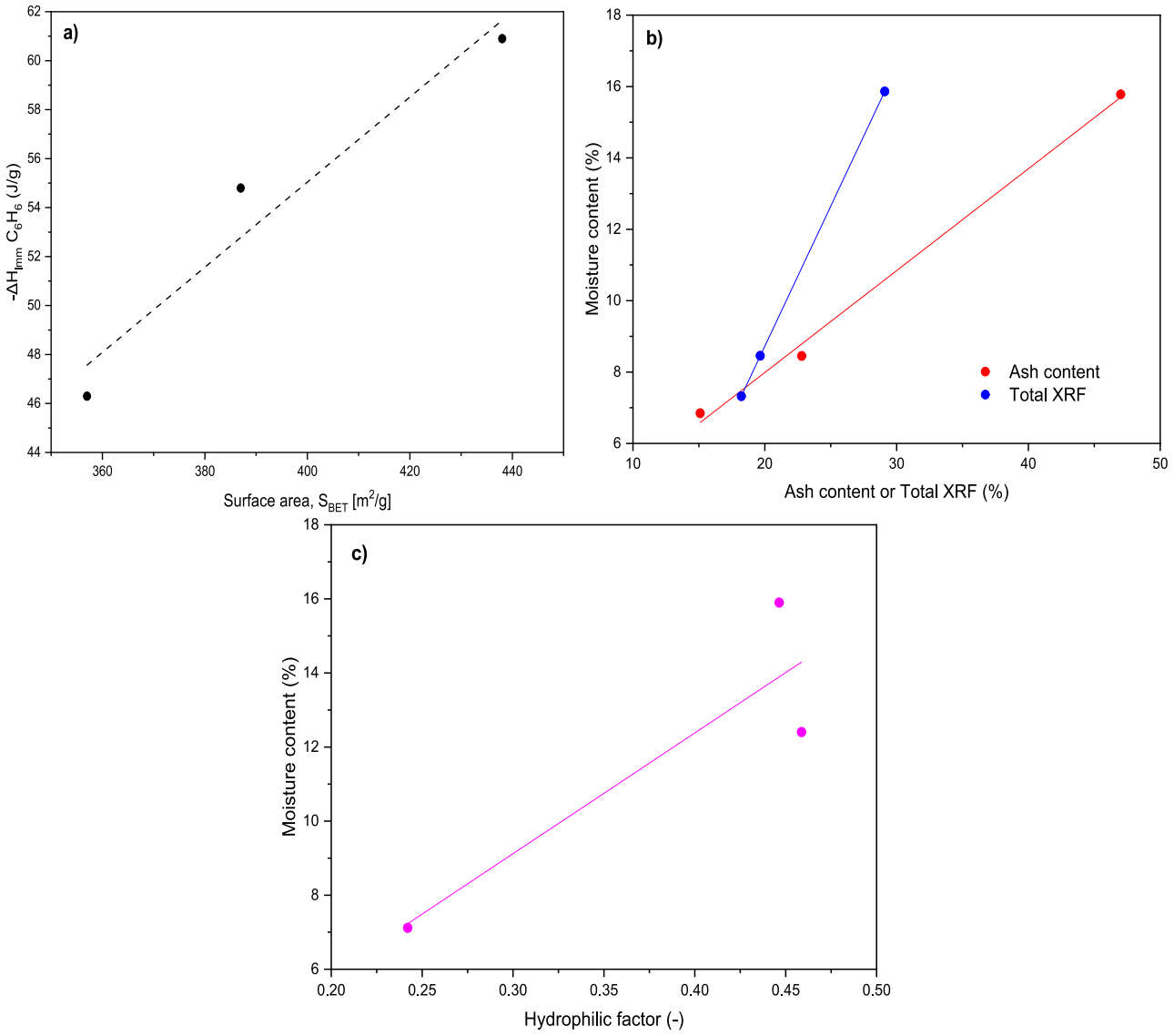

Fig. 8. Correlation between (a) surface area versus immersion enthalpy in benzene, (b) ash content, and total XRF versus moisture content, and (c) hydrophilic factor versus moisture content.

other words, the Toth equation produced the best fit with the least error compared to other isotherm models, describing adsorption on a heterogeneous surface. The generic mathematical representation is presented as below [74]:

$$q = \frac{q_{mT} b_T p}{(1 + (b_T p)^{n_T})^{1/n_T}} \tag{10}$$

where:

q_{mT} – maximum adsorption capacity, [mmol/g]
b_T – Toth constant, [bar^{-1}]
n_T – heterogeneity factor

Table 7 presents the parameters of the Toth isotherm for all tested gases at the temperature of the adsorption process of 25 °C. The parameter n_T is being used as a heterogeneity factor, and it ranges from 0 to 1. A value of 1 corresponds to a homogeneous surface, implying that adsorption sites on the surface are equivalent and have the same adsorption energy, consistent with the assumptions of a homogeneous surface. On the other hand, a lower value of n_T indicates greater surface heterogeneity, where adsorption sites on the surface vary in terms of their adsorption energies and characteristics.

3.3.4. Selectivity studies

The preferential adsorption of CO_2 compared to other gases such as N_2 and CH_4, is a crucial factor in several industrial and environmental contexts. These include applications like carbon capture and storage, natural gas purification, and hydrogen production. This level of selectivity is of utmost importance in mitigating greenhouse gas emissions, optimizing energy efficiency, and advancing the overall sustainability of many processes and sectors.

The widely used IAST, as established by Myers and Prausnitz [35] is extensively utilized in the field to accurately predict adsorption selectivity and mixed-gas adsorption isotherms. This theory relies on pure-component isotherms and offers reasonable accuracy over a range of systems. The selectivity ratio between CO_2 and different gases for an equimolar binary mixture at a temperature of 298 K and at a certain pressure was calculated using Eq. (9). All calculations were performed for the sample FERN800, which possessed the best sorption capabilities.

$$S_{IAST(EQM)} = \frac{q_{CO_{2(p)}}}{q_{G_{(p)}}} \tag{13}$$

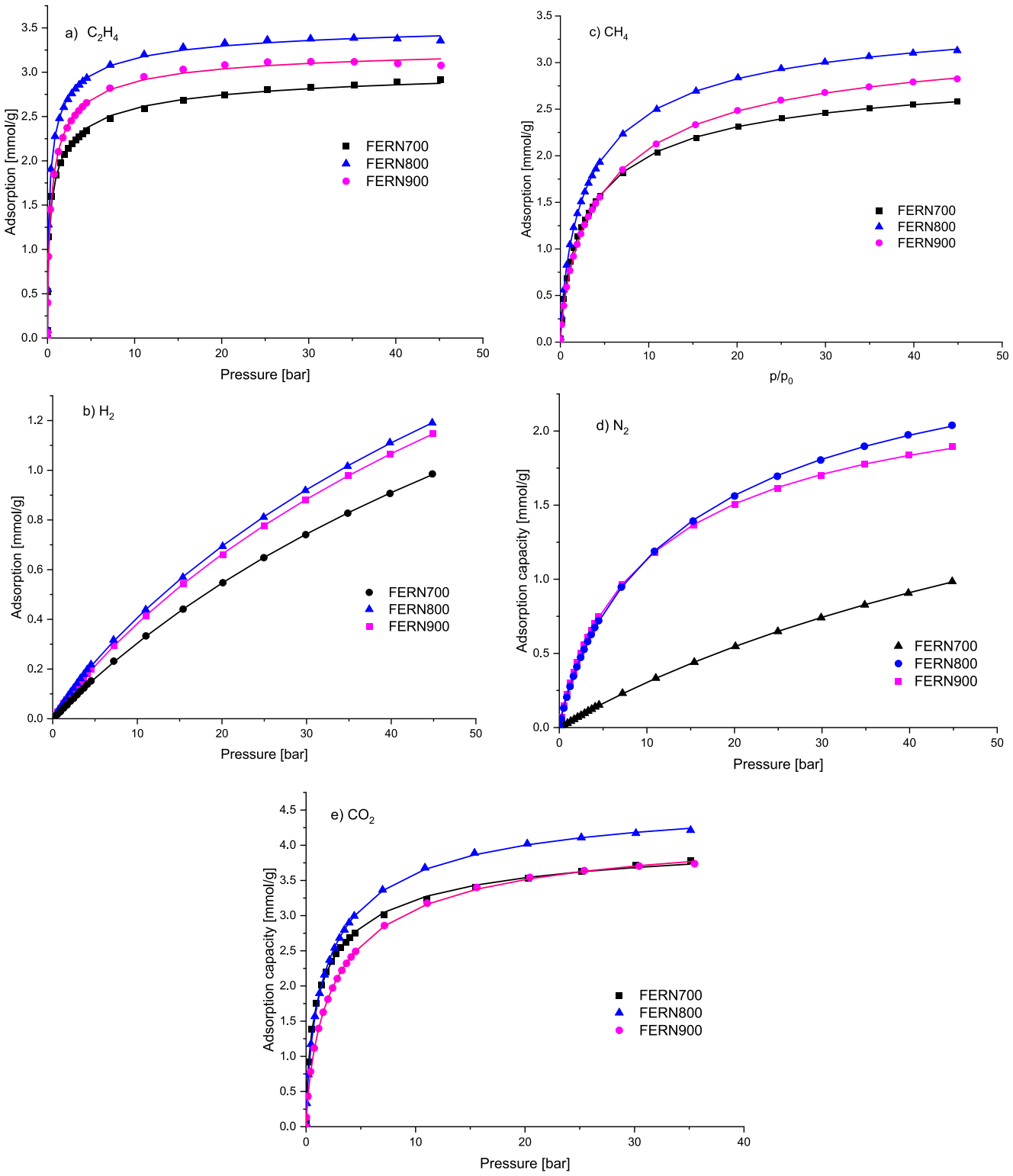

Fig. 9. High-pressure adsorption of **(a)** ethene, **(b)** hydrogen, **(c)** methane, **(d)** nitrogen, **(e)** carbon dioxide.

$$S_{(CO_{2_{10}}or15)} = \frac{q_{CO_2(p_{CO2})}}{p_{CO_2}} : \frac{q_{N_2(p_{N2})}}{p_{N_2}} \quad (14)$$

where: $q_{CO_{2(p)}}$ is the adsorption capacity at the same partial pressure p of CO_2 and N_2/CH_4.

The FERN800 adsorbent demonstrated a selectivity ratio of 551, 520, and 502 for CO_2 over N_2/CH_4 at a pressure of 0.1 bar, respectively. The correlations are shown in Fig. 13. However, at a pressure of 35 bar, the selectivity ratio decreased significantly to 77, 47, and 28. The CO_2/N_2 selectivity observed in this study was found to be much greater than those reported in previous literature. The selectivity seen may be attributed to the distinct chemical and physical characteristics shown by carbon dioxide. CO_2 molecules exhibit greater size and stronger polarizability in comparison to nitrogen N_2 and CH_4 molecules. As a result, adsorbents and membranes can be designed to preferentially attract and

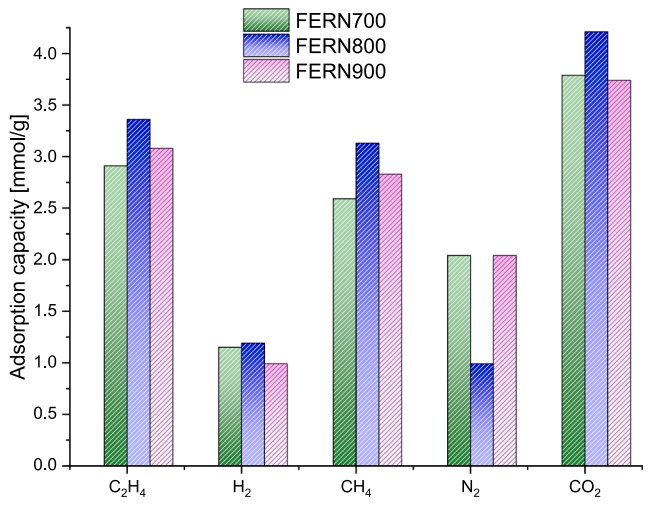

Fig. 10. Histogram of the adsorption capacities of each studied gaseous molecules for the AC materials.

Table 6
Comparison of C_2H_4, H_2, CH_4, and CO_2 uptake on different adsorbents at 45 bar and 25–35 °C.

Adsorbent	Gas uptake [mmol/g]				Reference
	C_2H_4	H_2	CH_4	CO_2	
FERN800	3.36	1.19	3.14	4.21	This study
Activated carbon	–	–	–	10.99	[67]
OP-H_3PO_4	–	0.99	–	–	[68]
ZSM-5	–	–	0.97	3.98	[69]
AC	–	0.5	–	–	[70]
ZIF-8	–	0.80	4.72	–	[71]

capture CO_2 while allowing the passage of smaller, nonpolar molecules like N_2 and CH_4.

The most frequently discussed problem is the adsorption capture of CO_2 from waste gases. There is usually 15 % CO_2 in such gases. Calculating the selectivity for the binary gas mixture CO_2 and N_2 containing 15 % CO_2 and 85 % N_2 is relevant. Fig. 14 shows the selectivity of CO_2 adsorption over N_2 denoted CO_2 vs N_2 as a function of pressure. The highest selectivity CO_2 vs N_2 was achieved over FERN 700 carbon. It was very high and was equal to 146 at 1 bar. The selectivity values decreased rapidly with increasing pressure up to 10 bar and then decreased very gradually. At 10 bar, the selectivity was 45, and at 25 bar, it was 27. These values were very high compared to the different published literature [75]. The selectivity O_2 vs N_2 was equal to 12.3 and 11 for 1 and 25 bar, respectively.

Also, an important binary system in the separation and purification process of pre-dried landfill gas (biogas) involves a CO_2/CH_4 mixture with molar compositions ranging from 25–50 % for CO_2 and 50–75 % for CH_4. Fig. 15 shows the selectivity of CO_2 adsorption over CH_4 as a function of temperature for a binary mixture containing 50 % CO_2 and 50 % CH_4. Belmabkhout, et al. [76] demonstrated selectivity of CO_2 vs N_2 in the range 2–5 at the pressure of 1 bar and 2—6 at the pressure of 25 bar. The separation of CO_2 from CO_2/CH_4 mixtures has undergone both experimental and theoretical scrutiny, involving alternative adsorbents such as MOFs. At a pressure of 20 bar the selectivity CO_2 vs N_2 was achieved 3 for IRMOF-1 [77] and for MOF-508b [78].

It is widely acknowledged that the composition of natural gas is contingent upon the geographic region of the deposit. It is noteworthy to emphasize that gas wells originating from the same field may exhibit divergent compositions. As a prominent contaminant in natural gas feeds, carbon dioxide must be effectively removed, as its presence reduces the energy content of the gas and influences the selling price of natural gas [79]. Selectivity studies commonly consider a CO_2 content of 5 % in natural gas [37,38]. The figure illustrates the selectivity of CO_2 adsorption over CH_4 for a binary mixture containing 5 % CO_2 (see Fig. 16). The achieved selectivity separation ranged from 4.0 to 8.6 at a pressure of 1 bar and from 11.0 to 15.6 at a pressure of 25 bars. These values compare favorably with those reported by other authors (8.0 and 9.6) [38] and (2.3, 3.3, 4.7, 6.6, 59.9) [37]. Activated carbons produced by us exhibited good selectivity for CO_2 vs CH_4 and can be applied for capturing carbon dioxide from natural gas.

The discussion revolves around the CO_2 vs. H_2 uptake for activated carbons produced from fern leaves presented in Fig. 17. The concentration typical for syngas was considered (20 % CO_2 and 80 % H_2). The selectivity of CO_2 over H_2 for FERN 700 demonstrated a remarkably high value, reaching 90 at a pressure of 1 bar. According to our knowledge, such high selectivity of CO_2 over H_2 was not achieved before. The selectivity CO_2 vs H_2 for FERN 800 and FERN 900 at 1 pressure was about 63. At 25 bar the selectivity for all carbon produced from CO_2 fern leaves was about 18. Belmabkhout et al. [80] achieved CO_2 vs H_2 selectivity at about 32 and 55 at pressure 1 bar and 25 respectively. Akten et al. [81] showed CO_2 vs H_2 selectivity at about 70 and 50 at pressure 1 bar and 25, respectively. The results imply that these adsorbents have promising capabilities for selectively extracting CO_2 from syngas, especially in the context of applications related to pre-combustion CO_2 capture. This is particularly relevant in processes where precise removal of CO_2 from syngas is essential, as seen in pre-combustion CO_2 capture. Such utilization contributes significantly to enhancing the system's overall efficiency and environmental impact.

The feasibility of utilizing activated carbons derived from fern leaves for the capture of C_2H_4 from natural gas was also explored. The results of IAST calculations are shown in Fig. 18. The selectivity for C_2H_4 vs CH_4 is presented in the figure. At a pressure of 1 bar, the values varied from 3 to 6, while at a pressure of 25 bars, they were approximately 1.3. Literature reports regarding the selectivity of C_2H_4 adsorption over CH_4 testing are infrequent. Masoudi-Nejad and Fatemi [38] achieved selectivity for C_2H_4 vs CH_4 values of approximately 7, while Liu et al. [82] reported values around 14.

3.3.5. *Stability studies under adsorption–desorption cycles*

A thorough understanding of activated carbons' stability under changing adsorption–desorption cycles conditions is essential for the optimal usage of these adsorbents to achieve the greatest affinity towards certain gases. In that case for CO_2, H_2, CH_4, C_2H_4, as was presented in section 3.3.4. The aforementioned cycles imitate the operational dynamics of capture systems in the real world, whereby the adsorbent material undergoes repetitive exposure to the gaseous mixture and subsequent regeneration. The repetitive nature of this operational process is crucial in evaluating the extended-term efficacy and durability of the materials.

Hence, an investigation was conducted to assess the reusability of the FERN800 by the execution of twenty adsorption–desorption cycles at a temperature of 298 K. The adsorption isotherms for the 1st, 5th, 10th, 15th, 20th data points are shown in Fig. 19. After a total of twenty repetitions, there was no observable change in the CO_2, H_2, CH_4, and C_2H_4 uptake. The maximum value of the standard deviation was 0.14. Based on the aforementioned evidence, it can be inferred that the FERN800 shows exceptional stability as an adsorbent material.

3.3.6. *Hypothetical economic analysis to produce activated carbon from fern leaves*

This study presents a hypothetical economic analysis for producing activated carbon from fern leaves, utilizing biomass waste from the pharmaceutical industry in Vietnam. Vietnam was selected as the location for constructing the production facility due to its favorable economic conditions, including low labor costs, availability of raw materials, and supportive government policies for industrial development. We thoroughly evaluate the various cost components involved in

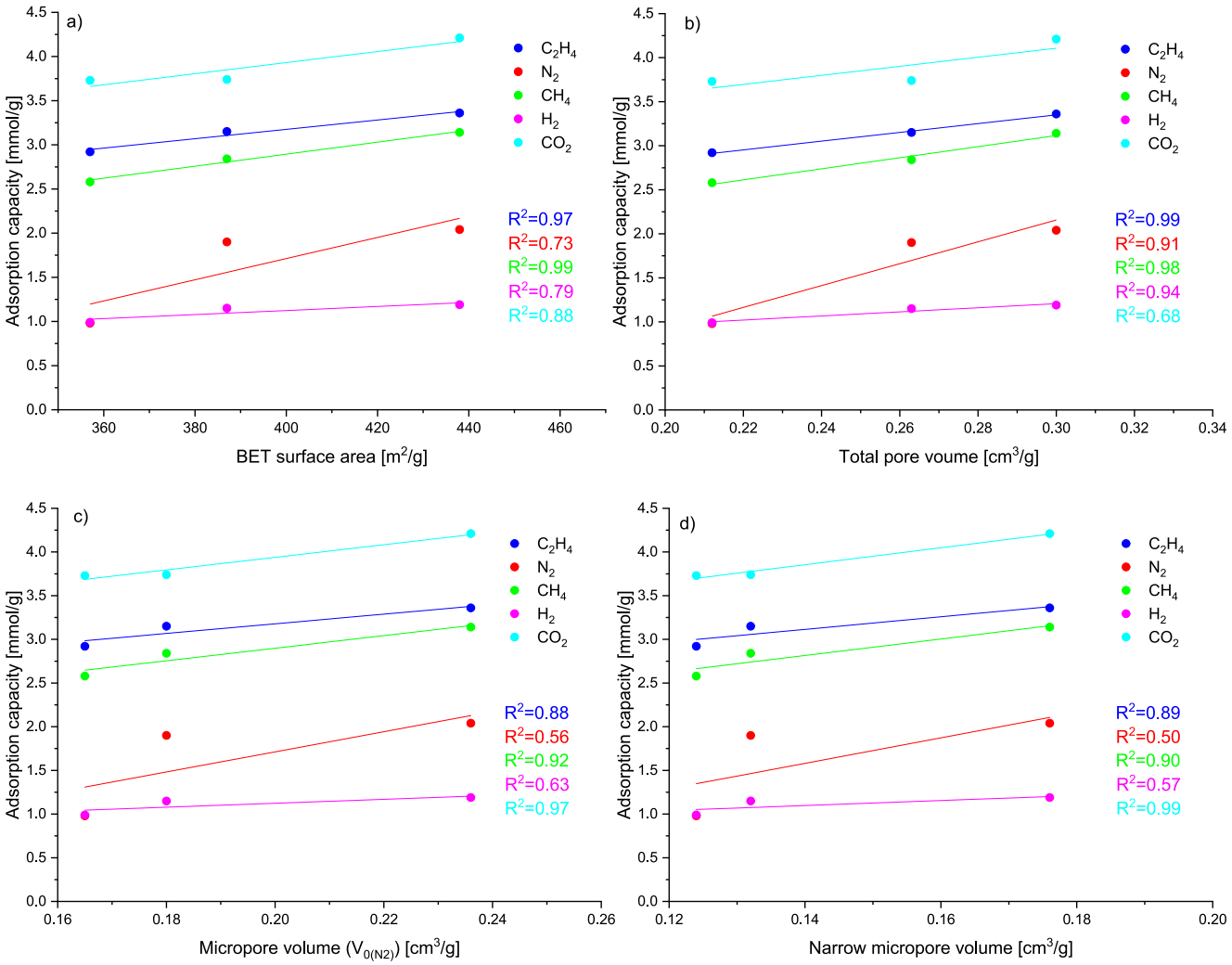

Fig. 11. Correlation between textural parameters, (a) BET surface area, (b) total pore volume, (c) micropore pore volume obtained from N_2 adsorption and (d) narrow micropore volume (<0.8 nm) and the amount adsorbed of ethene, hydrogen, methane, nitrogen, carbon dioxide on FERN materials.

constructing and operating a production facility. The analysis encompasses installation costs, material processing, equipment investment, staffing, utilities, maintenance, quality control, and logistics. By examining these aspects, we aim to provide a comprehensive understanding of this innovative production method's economic feasibility and market competitiveness. All costs outlined and described below have been converted into both Euro (€) and Chinese Yuan (CNY), using the exchange rate: 1 Euro (€) = 7.80 Chinese Yuan (CNY). This ensures consistency in financial planning and management across both currencies.

- **Biomass Source: Fern Leaves from Pharmacy Industry**

Fern leaves are acquired as biomass waste from the pharmacy industry, offering a sustainable and cost-effective raw material for activated carbon production. This sourcing strategy aligns with environmental sustainability goals while leveraging readily available biomass.

- **Installation and Facility Setup**

The initial phase involves the establishment of a production facility equipped with reactors, dryers, grinders, and other essential machinery (see Table 8). This encompasses site preparation, building construction, and installation of equipment necessary for the activation process.

- **Processing of Materials**

Processing fern leaves for activation involves essential steps such as cleaning, drying, and grinding to optimize material suitability for subsequent activation processes. The annual cost associated with these critical processes amounts to approximately 3000 € (23400 CNY). This investment ensures that raw materials are prepared to meet quality standards, supporting efficient production and maintaining product integrity throughout the activation process. The total investment in equipment amounts to approximately 97,000 € (756600 CNY). This includes essential machinery such as reactors, dryers, grinders, and other necessary equipment (see Table 9). Additionally, annual depreciation costs are estimated at 8000 € (62400 CNY), spread evenly over a 10-year period. Depreciation reflects the gradual wear and tear of equipment over time, ensuring financial planning aligns with long-term asset management strategies. These figures underscore the importance of capital expenditure and ongoing maintenance to sustain operational efficiency and profitability.

- **Staffing**

Operational efficiency depends heavily on skilled personnel overseeing production activities. Production operators manage machinery to meet production targets, while supervisors coordinate activities to ensure quality and safety standards are upheld. Support staff, including

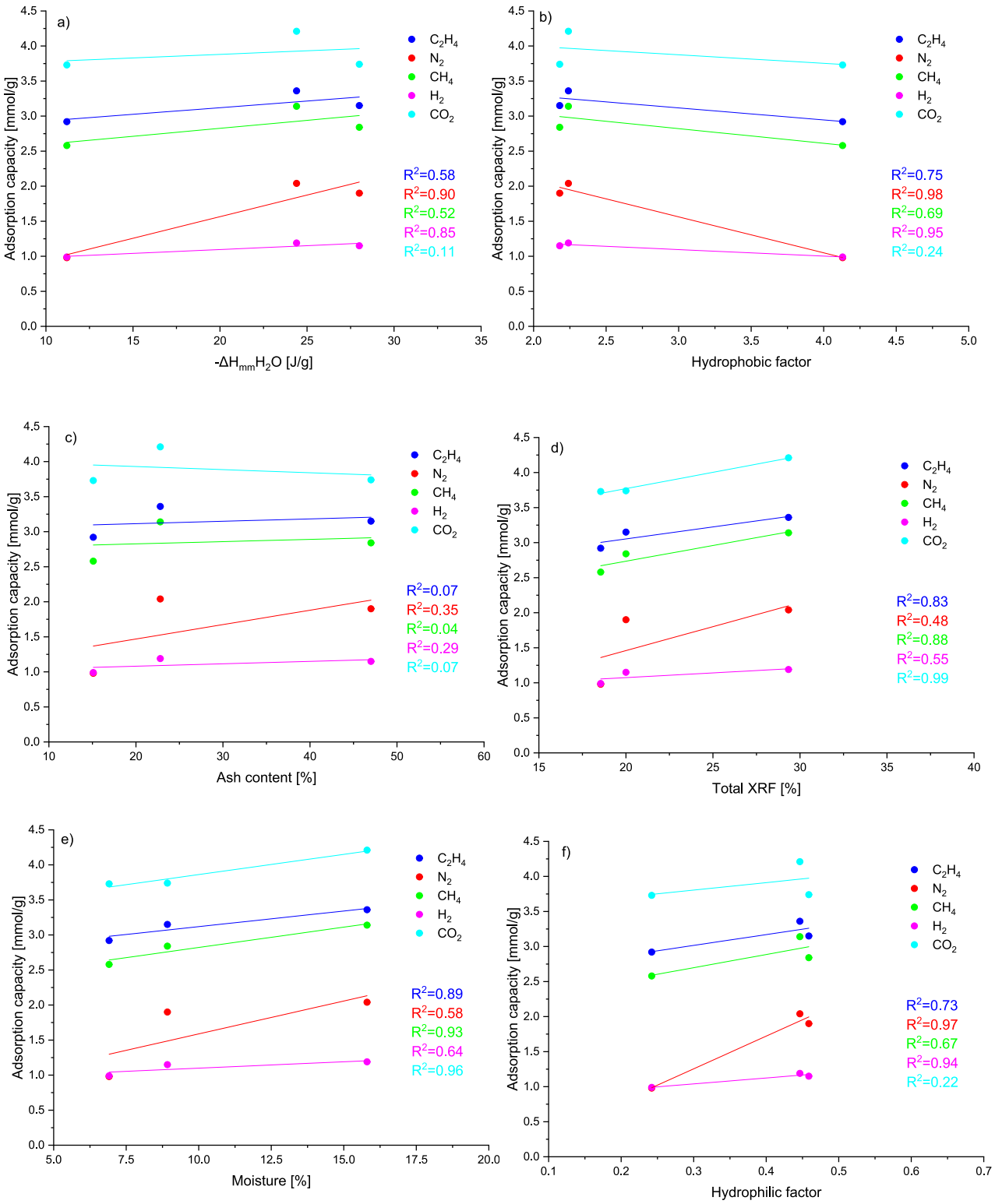

Fig. 12. Correlation between chemical parameters, **(a)** immersion enthalpy in water, **(b)** hydrophobic factor, **(c)** ash content, **(d)** total inorganic atoms by XRF, **(e)** moisture, **(f)** hydrophilic factor and the amount adsorbed of ethene, hydrogen, methane, nitrogen, carbon dioxide on FERN materials.

maintenance technicians and logistics coordinators, play essential roles in equipment upkeep and efficient material handling. Together, they maintain high productivity and effectively achieve operational goals (Table 10). Annual Cost: Approximately 15,000 € (117000 CNY) for three production operators, supervisors, and support staff.

- **Utilities and Energy**

Substantial utility expenses are necessary due to energy-intensive processes. Managing electricity, water, and gas costs effectively is crucial for maintaining operational sustainability and controlling overhead costs. Efficient utilization of utilities supports cost-effective production and environmental sustainability goals (Table 11). Total Annual Cost for Utilities: Approximately €2800 (21840 CNY).

Table 7
Toth isotherm parameters for FERN materials.

Sample	q_{mT} [mmol/g]	b_T [bar^{-1}]	n_T
CO_2			
Fern_700	4.631	3.181	0.478
Fern_800	5.115	1.339	0.573
Fern_900	4.62	0.764	0.617
H_2			
Fern_700	5.072	0.01	0.657
Fern_800	6.284	0.01	0.581
Fern_900	3.477	0.01	0.851
CH_4			
Fern_700	3.243	0.708	0.575
Fern_800	3.886	0.698	0.592
Fern_900	3.689	0.431	0.602
C_2H_4			
Fern_700	3.413	40.295	0.369
Fern_800	3.786	30.984	0.432
Fern_900	3.454	9.623	0.51
N_2			
Fern_700	3.458	0.01	0.854
Fern_800	2.753	0.126	0.696
Fern_900	3.262	0.094	0.679

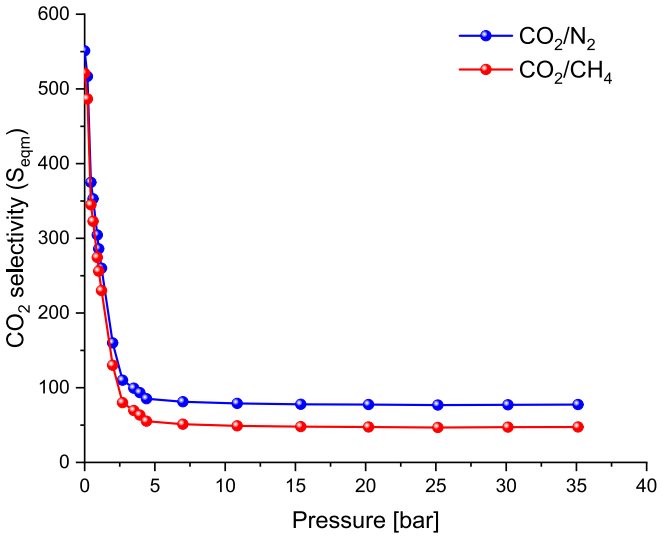

Fig. 13. The CO_2 over N_2, and CH_4 selectivity as a function of pressure at 298 K for FERN800.

- **Maintenance and Repairs**

Routine maintenance and occasional repairs are critical for ensuring equipment reliability. Properly maintained equipment reduces downtime, enhances operational efficiency, and extends equipment lifespan. By conducting regular inspections and addressing issues promptly, business can minimize unexpected breakdowns and maintain consistent production output. Annual Cost: Approximately 1000 € (7800 CNY).

- **Quality Control**

Stringent quality control measures are crucial to ensure product efficacy and compliance with industry standards. By investing approximately 500 € (3900 CNY) annually into quality assurance processes,

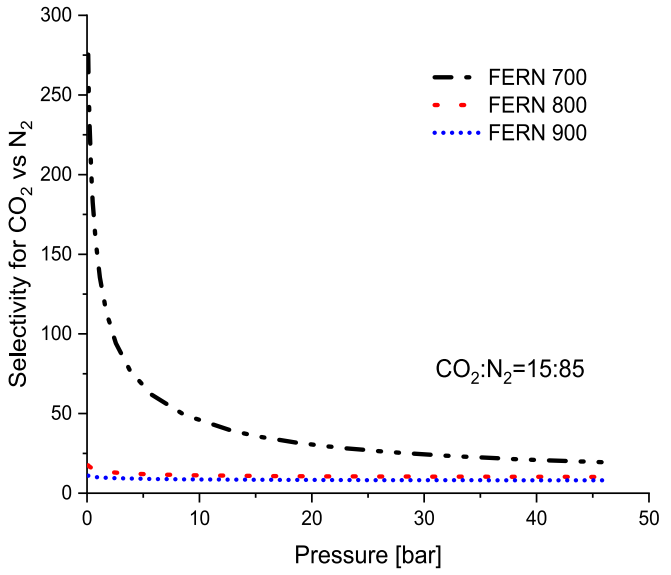

Fig. 14. The CO_2 over N_2, selectivity for flue gas composition as a function of pressure at 298 K.

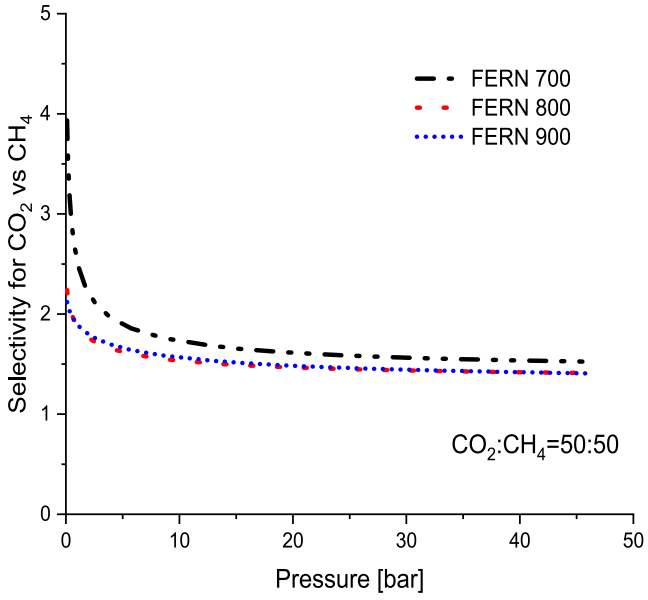

Fig. 15. The CO_2 over CH_4, selectivity for biogas composition as a function of pressure at 298 K.

business can maintain high product standards, customer satisfaction, and regulatory compliance. This proactive approach helps identify and rectify potential issues early, ensuring consistent quality and reliability in the final product.

- **Storage, Transportation, and Packaging**

Efficient logistics management plays a pivotal role in handling raw materials and distributing finished products effectively. Allocating 1000 € (7800 CNY) annually for storage ensures proper inventory management and preservation of materials. Additionally, dedicating 2000 € (15600 CNY) annually towards transportation and packaging facilitates timely delivery and maintains product integrity. The total annual logistics cost of 3000 € (23400 CNY) supports streamlined operations, ensuring smooth transitions from production to distribution.

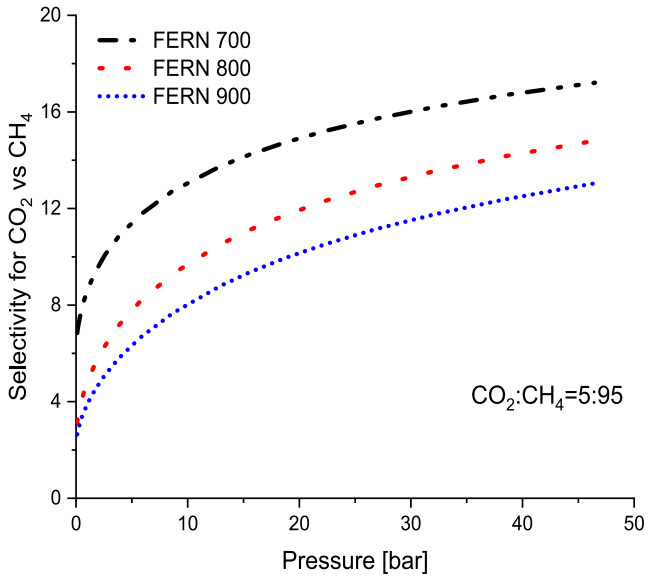

Fig. 16. The CO_2 over CH_4, selectivity for natural gas composition as a function of pressure at 298 K.

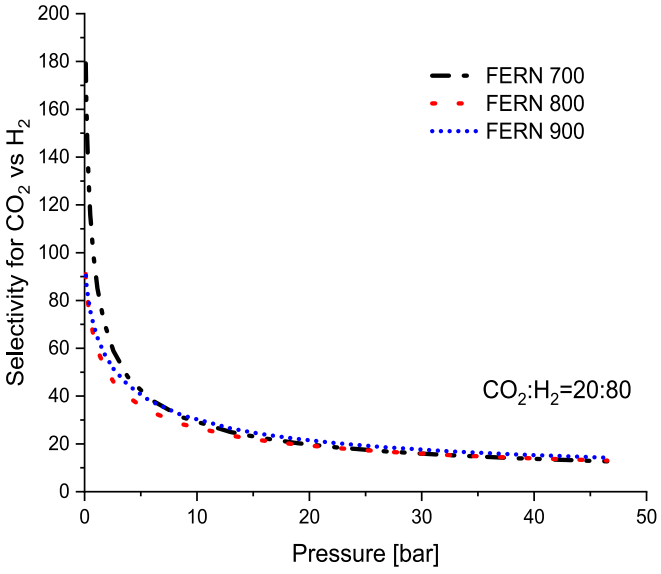

Fig. 17. The CO_2 over H_2, selectivity for syn gas composition as a function of pressure at 298 K.

- **Total Annual Production Costs**

Summing up all annual expenses results in total annual production costs amounting to approximately 122,300 € (953940 CNY). These costs encompass expenditures across staffing, utilities, maintenance, quality control, logistics, and other operational essentials. Managing these costs effectively is crucial for budgetary control and sustaining operational efficiency throughout the production cycle.

- **Determining the Price per Kilogram of Activated Carbon**

Ng et al. [83] explored the production costs associated with activated carbon derived from pecan shells, reporting a range of 2.34 € (18.25 CNY) to 2.49 € (19.42 CNY) per kilogram depending on the activation method used. Lima et al. [84] focused on producing activated carbon from organic waste through physical activation, achieving a competitive

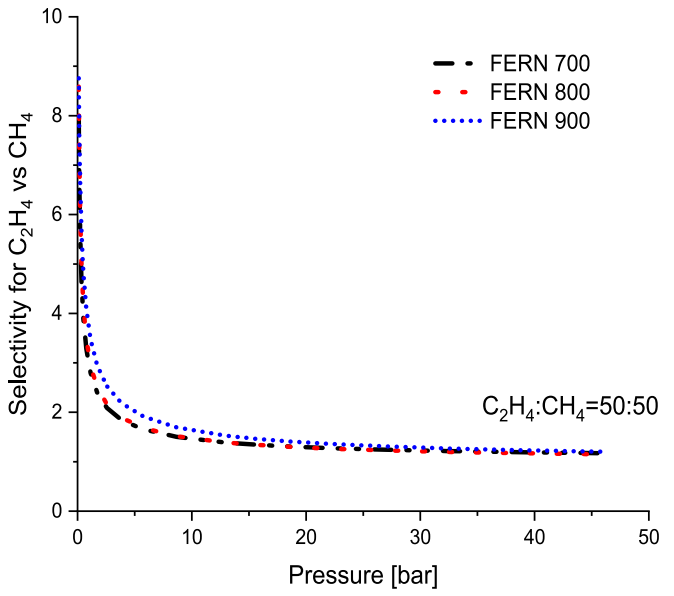

Fig. 18. The CO_2 over H_2, selectivity for syn gas composition as a function of pressure at 298 K.

cost of 1.24 € (9.67 CNY) per kilogram assuming no raw material expenses. In contrast, Stavropolous et al. [85] provided comparative cost analyses for activated carbon sourced from various materials: used tires (9.81 € (76.52 CNY) /kg), wood (5.49 € (42.82 CNY)/kg), and lignite (4.62 € (36.04 CNY)/kg).

Given an annual production volume of 50,000 kg of activated carbon from fern leaves, the calculated production cost is approximately 2.45 € per kilogram, based on total annual production costs of 122,300 €.

$$Price\ per\ Kilogram = \frac{Total\ \ Annual\ \ Production\ \ Costs}{Annual\ \ Production\ \ Volum} = \frac{122300}{50000} = 2.45€(19\mathbf{CNY})$$

Comparing this to Ng et al. [79] findings, our production costs align closely with their reported range. Lima et al. [37] lower cost for organic waste indicates their efficient production method, reflecting minimal raw material expenses. In contrast, the costs reported by Stavropolous et al. [85] highlight the variability and higher expenses associated with different feedstock materials.

In the economic context, particularly in China, competitive production costs are achieved through lower labor rates, favorable utility expenses, and efficient operational practices. While initial investments in facility setup and equipment are significant, ongoing costs are minimized, which supports profitability in the activated carbon market. Utilizing biomass waste as a raw material not only enhances cost-effectiveness but also aligns with sustainability goals. Strict adherence to quality control measures is essential for maintaining product reliability and competitiveness. Effective logistics management and prudent financial planning are critical for sustainable growth and profitability in the activated carbon production industry. This approach ensures that our production of activated carbon from fern leaves remains competitive and economically viable, reflecting our commitment to efficiency, sustainability, and high-quality standards in the market.

4. Conclusions

The research conducted was primarily centered on investigating the feasibility of producing activated carbons from the widely available fern leaves. The objective was to generate materials that exhibit improved hydrogen, ethene, methane, and carbon dioxide at high pressures, involving the use of phosphoric acid (H_3PO_4) and thermal conversion at three distinct temperatures, namely 700, 800, or 900 °C. The porous structure of the produced ACs has been examined to investigate the effect of chemical and textural parameters on sorption capabilities. The experimental results have shown that the activated carbons synthesized

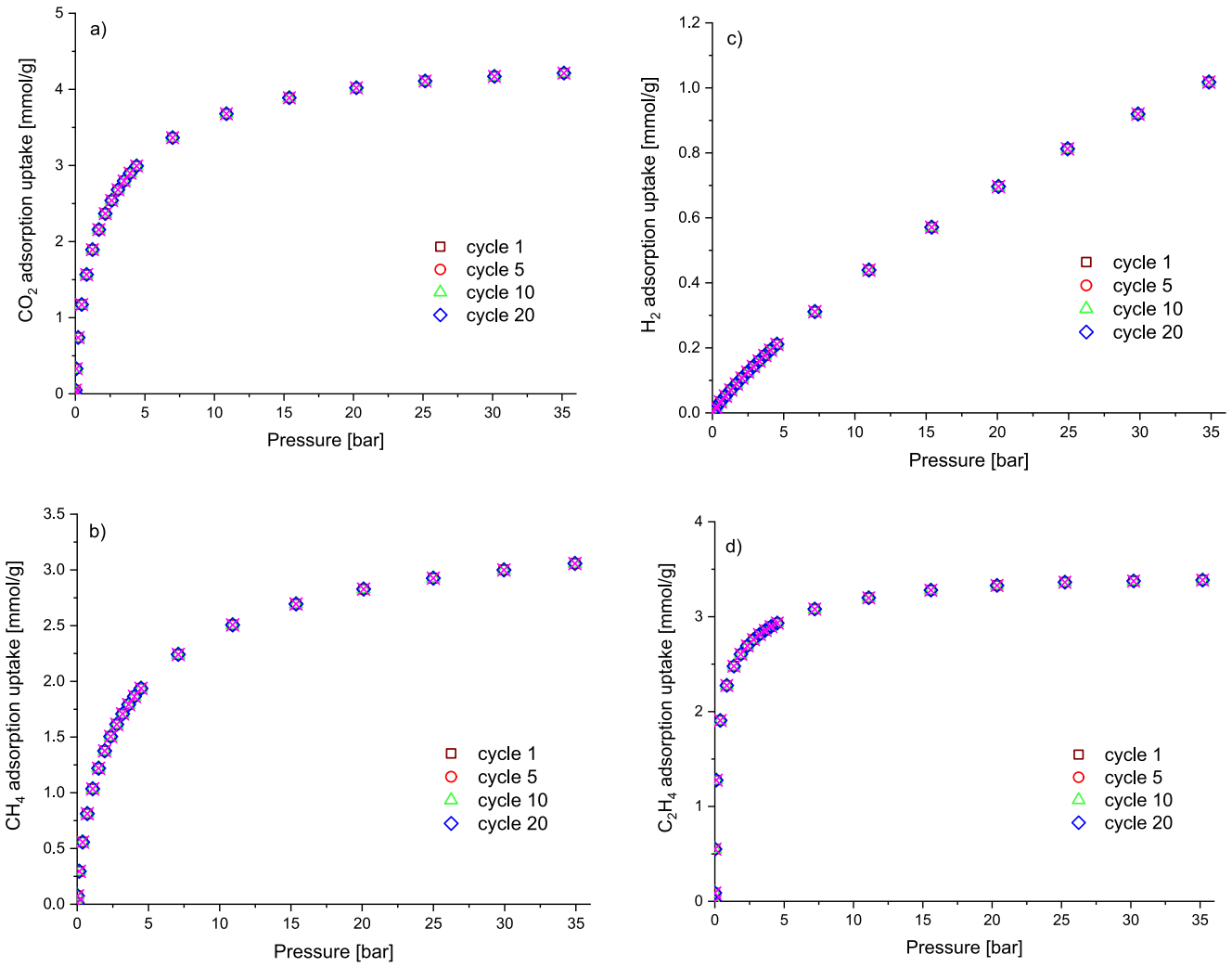

Fig. 19. (a) CO_2, (b) CH_4, (c) H_2, (d) C_2H_4 adsorption isotherms for FERN800 at 298 K in 1st, 5 th, 10th, and 20th, cycles.

Table 8
Installation and facility setup cost.

Cost component	Estimated cost (€)	Estimated cost (CNY)
Facility Setup	40,000	312,000
Construction Materials	10,000–20,000	78,000–156,000
Labor	8000–15,000	62,400–117,000
Design	2000–4000	15,600–31,200
Technical Installations	3000–5000	23,400–39,000
Fire Safety Measures	500–1000	3900–7800
Permits and Certificates	500–1000	3900–7800

Table 9
Materials cost.

Equipment	Estimated cost (€)	Estimated cost (CNY)
Horizontal Tube Furnace	15,000	117,000
Stainless Steel Reactors	30,000	234,000
Drying and Grinding Equipment	15,000	117,000
Filtration and Washing Units	7000	54,600
Quality Control Instruments	3000	23,400
Packaging Machinery	7000	54,600
Storage Facilities	20,000	156,000

at a temperature of 800 °C (FERN800) exhibit the highest values for specific surface area, total pore and micropore volume (438 m^2/g, 0.300 cm^3/g, and 0.236 cm^3/g). Consequently, the FERN800 adsorption

Table 10
Human resources cost.

Staff role	Estimated hourly rate (€)	Estimated hourly rate (CNY)
Production Operators	2–4	16–31
Supervisors	4–6	31–47
Support Staff	1–2	8–16

capacity of C_2H_4, H_2, CH_4, and CO_2 uptake of 3.36, 1.19, 3.14, and 4.21 mmol/g at a pressure of 45 bar, respectively. Furthermore, the influence of textural and chemical properties on the adsorption performance of ACs was examined, which is impacted by a multitude of variables. The complexity of this phenomena may be attributed to several factors, such as the size and configuration of the gas particles, their polarity, and the specific mechanism occurring at the adsorption sites inside the material. The FERN800 exhibited the greatest selectivity towards CO_2 in binary mixtures of $N_2/CH_4/H_2$, as calculated by the IAST equation for equimolar. At a temperature of 25 °C, the selectivity ratio values for CO_2 over $N_2/CH_4/H_2$ at a pressure of 0.1 bar were found to be 551, 520, and 502, respectively. Additionally, the cyclic stability studies involving the adsorption and desorption of CO_2, H_2, CH_4, and C_2H_4, on FERN800 demonstrated favorable reversibility and reusability over a span of 20 cycles at ambient temperature. Very high selectivity: 146 at 1 bar for CO_2 over N_2 for flue gas (15 % CO_2) was achieved. The selectivity of CO_2

Table 11
Utilities and energy cost.

Utility	Unit cost (€)	Unit cost (CNY)	Annual consumption	Annual cost (€)	Annual cost (CNY)
Electricity	0.05–0.07 per kWh	0.39–0.55 per kWh	20,000 kWh	1000–1400	7800–10920
Water	0.20–0.30 per m^3	1.56–2.34 per m^3	3000 m^3	600–900	4680–7020
Gas	0.80–1.20 per m^3	6.24–9.36 per m^3	1500 m^3	1200–1800	9360–14040

(20 %) over H_2 reached 90 at a pressure of 1 bar. Such a high value has not been described up to now. Activated carbons produced from fern leaves activated by H_3PO_4 can also capture carbon dioxide from biogas, natural gas, and ethane from natural gas. Additionally, the calculated cost of producing 1 kg of the activated carbon was found to be 2.45 € (19 CNY), positioning it competitively in the market.

Furthermore, discussing our study's limitations and suggesting future research directions is crucial for acknowledging uncertainties and guiding further exploration. This approach aims to enhance the validity of our findings and pave the way for future advancements in the field.

- **Limitations:**
  - **Scale-Up Challenges**: While our laboratory-scale synthesis of activated carbons (ACs) from fern leaves has shown promising results, scaling up the process to industrial levels presents several challenges. Ensuring uniform impregnation of H_3PO_4 and maintaining consistent thermal conditions during the carbonization process are critical factors that need to be addressed for successful large-scale production.
  - **Purity of Gases**: The gases used in our adsorption experiments were of high purity. However, real-world gas streams often contain impurities that could affect the adsorption performance of ACs. The impact of such impurities on the adsorption capacity and selectivity of our fern-derived ACs warrants further investigation.
  - **Operational Conditions**: Our experiments were conducted at a constant temperature of 25 °C. Industrial processes, however, operate over a range of temperatures and pressures. To fully understand the practical applicability of our ACs, it is crucial to investigate their performance under varying operational conditions.
- **Future Research Directions:**
  - **Scaling Up Production**: Future research should prioritize optimizing the synthesis process for large-scale production. This includes exploring alternative activation methods that are both cost-effective and environmentally friendly. Pilot-scale studies will be instrumental in addressing the challenges associated with scale-up.
  - **Impurity Effects**: Investigating the impact of common impurities present in gas streams on the adsorption performance of fern-derived ACs is essential. Such studies will provide insights into the robustness and reliability of these materials in industrial applications, where gas purity cannot always be guaranteed.
  - **Temperature and Pressure Variability**: Conducting adsorption experiments across a broader range of temperatures and pressures is necessary to assess the versatility and limitations of fern-derived ACs. Understanding how these materials perform under different operational scenarios will enhance their practical utility.
  - **Material Modification**: Exploring the modification of fern-derived ACs with other elements or compounds could enhance their adsorption properties. For instance, doping with metals or introducing additional functional groups may improve selectivity and capacity.

CRediT authorship contribution statement

Jarosław Serafin: Writing – review & editing, Writing – original draft, Visualization, Validation, Supervision, Project administration, Methodology, Investigation, Formal analysis, Data curation, Conceptualization. **Bartosz Dziejarski:** Writing – review & editing, Writing – original draft, Visualization, Validation, Methodology, Investigation, Formal analysis, Data curation. **Paola Rodríguez-Estupiñán:** Investigation, Formal analysis, Data curation. **Valentina Bernal Fernández:** Investigation, Formal analysis, Data curation. **Liliana Giraldo:** Writing – original draft, Formal analysis. **Joanna Sreńscek-Nazzal:** Writing – original draft, Investigation, Formal analysis, Data curation. **Beata Michalkiewicz:** Writing – original draft, Formal analysis, Data curation. **Juan Carlos Moreno-Piraján:** Writing – original draft, Supervision, Methodology, Formal analysis, Data curation.

Declaration of competing interest

The authors declare that they have no known competing financial interests or personal relationships that could have appeared to influence the work reported in this paper.

Data availability

Data will be made available on request.

References

[1] Feng S, Ngo HH, Guo W, Chang SW, Nguyen DD, Bui XT, et al. Biohydrogen production, storage, and delivery: a comprehensive overview of current strategies and limitations. Chem Eng J 2023:144669.
[2] Zhang H, Wang J, Zhao X, Yang J. Modeling a hydrogen-based sustainable multi-carrier energy system using a multi-objective optimization considering embedded joint chance constraints. Energy 2023;278:127643.
[3] Park J, Attia NF, Jung M, Lee ME, Lee K, Chung J, et al. Sustainable nanoporous carbon for CO_2, CH_4, N_2, H_2 adsorption and CO_2/CH_4 and CO_2/N_2 separation. Energy 2018;158:9–16.
[4] Lin Z, Yuan Z, Dai Z, Shao L, Eisen MS, He X. A review from material functionalization to process feasibility on advanced mixed matrix membranes for gas separations. Chem Eng J 2023:146075.
[5] Cheng J, Cheng X, Wang Z, Hussain MB, Wang M. Multifunctional carbon aerogels from typha orientalis for applications in adsorption: hydrogen storage, CO_2 capture and VOCs removal. Energy 2023;263:125984.
[6] Li M, Yin W, Pan J, Zhu Y, Sun N, Zhang X, et al. Hydrogen spillover as a promising strategy for boosting heterogeneous catalysis and hydrogen storage. Chem Eng J 2023:144691.
[7] Wang C, Liu K, Liu J. Toluene adsorption performance study of cathode air filter for high-power hydrogen fuel cell vehicles. Chem Eng J 2023;461:141782.
[8] Chi Y, Xu W, Xiao M, Wang Z, Zhang X, Chen Y. Fuel-cycle based environmental and economic assessment of hydrogen fuel cell vehicles in China. Energy 2023;282:128773.
[9] Abd AA, Othman MR, Shamsudin IK, Helwani Z, Idris I. Biogas upgrading to natural gas pipeline quality using pressure swing adsorption for CO_2 separation over UiO-66: experimental and dynamic modelling assessment. Chem Eng J 2023;453:139774.
[10] Mukhtar A, Ullah S, Inayat A, Saqib S, Mellon NB, Assiri MA, et al. Synthesis-structure-property relationship of nitrogen-doped porous covalent triazine frameworks for pre-combustion CO_2 capture. Energy 2021;216:119230.
[11] Shi J, Xu J, Cui H, Yan N, Zou J, Liu Y, et al. Synthesis of highly porous N-doped hollow carbon nanospheres with a combined soft template-chemical activation method for CO_2 capture. Energy 2023:128172.
[12] Pereira A, Ferreira AF, Rodrigues A, Ribeiro AM, Regufe MJ. Evaluation of the potential of a 3D-printed hybrid zeolite 13X/activated carbon material for CO_2/N_2 separation using electric swing adsorption. Chem Eng J 2022;450:138197.
[13] Serafin J, Dziejarski B. Activated carbons—preparation, characterization and their application in CO_2 capture: a review. Environ Sci Pollut Res 2023:1–55.
[14] Dziejarski B, Serafin J, Andersson K, Krzyżyńska R. CO_2 capture materials: a review of current trends and future challenges. Mater Today Sustain 2023:100483.
[15] Mikhaylov A, Moiseev N, Aleshin K, Burkhardt T. Global climate change and greenhouse effect. Entrepreneurship Sustainability Issues 2020;7(4):2897.
[16] Avtar R, Tripathi S, Aggarwal AK, Kumar P. Population–urbanization–energy nexus: a review. Resources 2019;8(3):136.
[17] Fuso Nerini F, Sovacool B, Hughes N, Cozzi L, Cosgrave E, Howells M, et al. Connecting climate action with other Sustainable Development Goals. Nat Sustainability 2019;2(8):674–80.

[18] Stocker T, editor. Climate change 2013: the physical science basis: Working Group I contribution to the Fifth assessment report of the Intergovernmental Panel on Climate Change. Cambridge University Press; 2014.
[19] Palm, R., Bolsen, T., Palm, R., & Bolsen, T. (2020). The Science of Climate Change and Sea-Level Rise. Climate Change and Sea Level Rise in South Florida: The View of Coastal Residents, 5-13.
[20] Serafin J, Ouzzine M, Xing C, El Ouahabi H, Kamińska A, Sreńscek-Nazzal J. Activated carbons from the Amazonian biomass andiroba shells applied as a CO_2 adsorbent and a cheap semiconductor material. J CO_2 Util 2022;62:102071.
[21] Nisbet EG, Fisher RE, Lowry D, France JL, Allen G, Bakkaloglu S, et al. Methane mitigation: methods to reduce emissions, on the path to the Paris agreement. Rev Geophys 2020;58(1):e2019RG000675.
[22] Ming T, Li W, Yuan Q, Davies P, De Richter R, Peng C, et al. Perspectives on removal of atmospheric methane. Adv Appl Energy 2022:100085.
[23] Abe JO, Popoola API, Ajenifuja E, Popoola OM. Hydrogen energy, economy and storage: review and recommendation. Int J Hydrogen Energy 2019;44(29): 15072–86.
[24] Reza MS, Yun CS, Afroze S, Radenahmad N, Bakar MSA, Saidur R, et al. Preparation of activated carbon from biomass and its' applications in water and gas purification, a review. Arab J Basic Appl Sci 2020;27(1):208–38.
[25] Lewoyehu M. Comprehensive review on synthesis and application of activated carbon from agricultural residues for the remediation of venomous pollutants in wastewater. J Anal Appl Pyrol 2021;159:105279.
[26] Chaparro-Garnica J, Salinas-Torres D, Mostazo-López MJ, Morallon E, Cazorla-Amorós D. Biomass waste conversion into low-cost carbon-based materials for supercapacitors: a sustainable approach for the energy scenario. J Electroanal Chem 2021;880:114899.
[27] Sreńscek-Nazzal J, Kamińska A, Miądlicki P, Wróblewska A, Kiełbasa K, Wróbel RJ, et al. Activated carbon modification towards efficient catalyst for high value-added products synthesis from alpha-pinene. Materials 2021;14(24):7811.
[28] Angın D, Altintig E, Köse TE. Influence of process parameters on the surface and chemical properties of activated carbon obtained from biochar by chemical activation. Bioresour Technol 2013;148:542–9.
[29] Rao RAK, Khan U. Adsorption studies of Cu (II) on Boston fern (Nephrolepis exaltata Schott cv. Bostoniensis) leaves. Appl Water Sci 2017;7:2051–61.
[30] Emrooz HBM, Maleki M, Shokouhimehr M. Excellent adsorption of orange acid II on a water fern–derived micro-and mesoporous carbon. J Taiwan Inst Chem Eng 2019;102:99–109.
[31] Serafin J, Narkiewicz U, Morawski AW, Wróbel RJ, Michalkiewicz B. Highly microporous activated carbons from biomass for CO_2 capture and effective micropores at different conditions. J CO_2 Util 2017;18:73–9.
[32] Serafin J, Kiełbasa K, Michalkiewicz B. The new tailored nanoporous carbons from the common polypody (Polypodium vulgare): the role of textural properties for enhanced CO_2 adsorption. Chem Eng J 2022;429:131751.
[33] Eriksson T. Ferns reawakened. Nature 2004;428(6982):480–1.
[34] Anderson OR. Physiological ecology of ferns: Biodiversity and conservation perspectives. Int J Biodiversity Conserv 2021;13(2):49–63.
[35] Flexas J, Carriquí M, Coopman RE, Gago J, Galmés J, Martorell S, et al. Stomatal and mesophyll conductances to CO_2 in different plant groups: underrated factors for predicting leaf photosynthesis responses to climate change? Plant Sci 2014;226: 41–8.
[36] Hu J, Liu Y, Liu J, Gu C, Wu D. High CO_2 adsorption capacities in UiO type MOFs comprising heterocyclic ligand. Microporous Mesoporous Mater 2018;256:25–31.
[37] Modak A, Bhaumik A. Porous carbon derived via KOH activation of a hypercrosslinked porous organic polymer for efficient CO_2, CH_4, H_2 adsorptions and high CO_2/N_2 selectivity. J Solid State Chem 2015;232:157–62.
[38] Liu X, Du J, Ye Y, Liu Y, Wang S, Meng X, et al. Boosting selective C_2H_2/CH_4, C_2H_4/CH_4 and CO_2/CH_4 adsorption performance via 1, 2, 3-triazole functionalized triazine-based porous organic polymers. Chin J Chem Eng 2022;42:64–72.
[39] Myers AL, Prausnitz JM. Thermodynamics of mixed-gas adsorption. AIChE Journal 1965;11(1):121–7.
[40] Barthlott W, Neinhuis C, Cutler D, Ditsch F, Meusel I, Theisen I, et al. Classification and terminology of plant epicuticular waxes. Bot J Linn Soc 1998;126(3):237–60.
[41] Węgle Aktywne - Metody Badań - Oznaczanie Zawartości Popiołu PN-84/C-97555/08, J.P.TadeuszL. Wierzbicki; 1985.
[42] Elmorsi TM. Equilibrium isotherms and kinetic studies of removal of methylene blue dye by adsorption onto miswak leaves as a natural adsorbent. J Environ Prot Ecol 2011;2:817–27. https://doi.org/10.4236/jep.2011.26093.
[43] Günay A, Arslankaya E, Tosun I. Lead removal from aqueous solution by natural and pretreated clinoptilolite: adsorption equilibrium and kinetics. J Hazard Mater 2007;146:362–71. https://doi.org/10.1016/j.jhazmat.2006.12.034.
[44] Ayawei N, Ekubo AT, Wankasi D, Dikio ED. Adsorption of congo red by Ni/Al – CO_3: equilibrium, thermodynamic and kinetic studies. Oriental J Chem 2015;31: 1307–18. https://doi.org/10.13005/ojc/310307.
[45] Jafari Behbahani T, Jafari Behbahani Z. A new study on asphaltene adsorption in porous media. Pet Coal 2014;5:459–66.
[46] Padder MS, Majunder CBC. Studies on Removal of As(II) and S(V) onto GAC/MnFe, Compos. Interface 2012;23:327–72. https://doi.org/10.1080/09276440.2016.1137715.
[47] Travis CC, Etnier EL. A survey of sorption relationships for reactive solutes in soil. J Environ Qual 1981;10:8–17. https://doi.org/10.2134/JEQ1981.00472425001000010002X.
[48] Serafin J, Dziejarski B, Solis C, de la Piscina PR, Homs N. Medium-pressure hydrogen storage on activated carbon derived from biomass conversion. Fuel 2024; 363:130975.
[49] Yaneva ZL, Koumanova BK, Georgieva NV. Linear regression and nonlinear regression methods for equilibrium modelling of p – nitrophenol biosorption by Rhyzopus oryzen: comparison of error analysic criteria. J Chem – NY 2013:517631. https://doi.org/10.1155/2013/517631.
[50] Thommes M, Kaneko K, Neimark AV, Olivier JP, Rodriguez-reinoso F, Rouquerol J, et al. Physisorption of gases, with special reference to the evaluation of surface area and pore size distribution (IUPAC Technical Report). Pure Appl Chem 2015;87: 1051–69. https://doi.org/10.1515/pac-2014-1117.
[51] Serafin J, Cruz Jr O. Promising activated carbons derived from common oak leaves and their application in CO_2 storage. J Environ Chem Eng 2022;10:104672.
[52] Yorgun S, Yıldız D. Preparation and characterization of activated carbons fromPaulownia wood by chemical activation with H_3PO_4. J Taiwan Inst Chem E 2015;53:122–31.
[53] Sych NV, Trofymenko SI, Poddubnaya OI, Tsyba MM, Sapsay VI, Klymchuk DO, et al. Porous structure and surface chemistry of phosphoric acid activatedcarbon from corncob. Appl Surf Sci 2012;261:75–82.
[54] Kumar A, Jena HM. Preparation and characterization of high surface area activated carbon from Fox nut (Euryale ferox) shell by chemical activation with H_3PO_4. Results Phys 2016;6:651–8.
[55] Neimark AV, Lin Y, Ravikovitch PI, Thommes M. Quenched solid density functional theory and pore size analysis of micro-mesoporous carbons. Carbon 2009;47(7): 1617–28.
[56] Shi K, Santiso EE, Gubbins KE. Bottom-up approach to the coarse-grained surface model: Effective solid–fluid potentials for adsorption on heterogeneous surfaces. Langmuir 2019;35(17):5975–86.
[57] Prahas D, Kartika Y, Indraswati N, Ismadji S. Activated carbon from jackfruit peel waste by H_3PO_4 chemical activation: pore structure and surface chemistry characterization. Chem Eng J 2008;140(1):32–42. https://doi.org/10.1016/j.cej.2007.08.032.
[58] Lu L, Sahajwalla V, Kong C, Harris D. Quantitative X-ray diffraction analysis and its application to various coals. Carbon 2001;39(12):1821–33.
[59] Zięzio M, Charmas B, Jedynak K, Hawryluk M, Kucio K. Preparation and characterization of activated carbons obtained from the waste materials impregnated with phosphoric acid(V). Appl Nanosci 2020;10(12). https://doi.org/10.1007/s13204-020-01419-6.
[60] Ouzilleau P, Gheribi AE, Chartrand P, Soucy G, Monthioux M. Why some carbons may or may not graphitize? The point of view of thermodynamics. Carbon 2019; 149:419–35.
[61] Putman KJ, Marks NA, Rowles MR, de Tomas C, Martin JW, Suarez-Martinez I. Defining graphenic crystallites in disordered carbon: moving beyond the platelet model; 2022. arXiv preprint arXiv:2212.06354.
[62] Jones DH, Srivastava KKP. Many-state relaxation model for the Mössbauer spectra of superparamagnets. Phys Rev B 1986;34(11):7542.
[63] Serafin J, Dziejarski B, Junior OFC, Sreńscek-Nazzal J. Design of highly microporous activated carbons based on walnut shell biomass for H_2 and CO_2 storage. Carbon 2023;201:633–47.
[64] Serafin J, Dziejarski B, Vendrell X, Kiełbasa K, Michalkiewicz B. Biomass waste fern leaves as a material for a sustainable method of activated carbon production for CO_2 capture. Biomass Bioenergy 2023;175:106880.
[65] Chen WH, Chen CY. Water gas shift reaction for hydrogen production and carbon dioxide capture: a review. Appl Energy 2020;258:114078.
[66] Singh M, Borkhatariya N, Pramanik P, Dutta S, Ghosh SK, Maiti P, et al. Microporous carbon derived from cotton stalk crop-residue across diverse geographical locations as efficient and regenerable CO_2 adsorbent with selectivity. J CO_2 Util 2022;60:101975.
[67] Singh VK, Kumar EA. Measurement and analysis of adsorption isotherms of CO_2 on activated carbon. Appl Therm Eng 2016;97:77–86.
[68] Bader N, Zacharia R, Abdelmottaleb O, Cossement D. How the activation process modifies the hydrogen storage behavior of biomass-derived activated carbons. J Porous Mater 2018;25:221–34.
[69] Ullah R, Saad MAHS, Aparicio S, Atilhan M. Adsorption equilibrium studies of CO_2, CH_4 and N_2 on various modified zeolites at high pressures up to 200 bars. Microporous Mesoporous Mater 2018;262:49–58.
[70] Park SJ, Lee SY, Yoo HM, Kim BJ. Influence of phosphoric acid treatment on hydrogen adsorption behaviors of activated carbons. Carbon Lett 2011;12(2): 112–5.
[71] Liu H, Pan Y, Liu B, Sun C, Guo P, Gao X, et al. Tunable integration of absorption-membrane-adsorption for efficiently separating low boiling gas mixtures near normal temperature. Sci Rep 2016;6(1):21114.
[72] Shao W, Zhang L, Li L, Lee RL. Adsorption of CO_2 and N_2 on synthesized NaY zeolite at high temperatures. Adsorption 2009;15:497–505. https://doi.org/10.1007/s10450-009-9200-y.
[73] Porter JF, McKay G, Choy KH. The prediction of sorption from a binary mixture of acidic dyes using single- and mixed-isotherm variants of the ideal adsorbed solute theory. Chem Eng Sci 1999;54:5863–85.
[74] Toth J. Calculation of the BET-compatible surface area from any type I isotherms measured above the critical temperature. J Colloid Interface Sci 2000;225:378–83.
[75] Muhammad R, Park J, Kim H, So SH, Nah YC, Oh H. Facile synthesis of ultrahigh-surface-area and hierarchically porous carbon for efficient capture and separation of CO_2 and enhanced CH_4 and H_2 storage applications. Chem Eng J 2023;473: 145344.
[76] Belmabkhout Y, Sayari A. Adsorption of CO_2 from dry gases on MCM-41 silica at ambient temperature and high pressure. 2: Adsorption of CO_2/N_2, CO_2/CH_4 and CO_2/H_2 binary mixtures. Chem Eng Sci 2009;64(17):3729–35.

[77] Yang Q, Zhong C. Electrostatic-field-induced enhancement of gas mixture separation in metal-organic frameworks: a computational study. ChemPhysChem: Eur J Chem Phys Phys Chem 2006;7(7):1417–21.
[78] Bastin L, Bárcia PS, Hurtado EJ, Silva JA, Rodrigues AE, Chen B. A microporous metal− organic framework for separation of CO_2/N_2 and CO_2/CH_4 by fixed-bed adsorption. J Phys Chem C 2008;112(5):1575–81.
[79] Shimekit B, Mukhtar H. Natural gas purification technologies-major advances for CO_2 separation and future directions. Adv Natural Gas Technol 2012;2012:235–70.
[80] Belmabkhout Y, Sayari A. Adsorption of CO {sub 2} from dry gases on MCM-41 silica at ambient temperature and high pressure. 2: Adsorption of CO {sub 2}/N {sub 2}, CO {sub 2}/CH {sub 4} and CO {sub 2}/H {sub 2} binary mixtures. Chem Eng Sci, 2009; 64.
[81] Akten ED, Siriwardane R, Sholl DS. Monte Carlo simulation of single-and binary-component adsorption of CO_2, N_2, and H_2 in zeolite Na-4A. Energy Fuel 2003;17 (4):977–83.
[82] Masoudi-Nejad M, Fatemi S. Thermodynamic adsorption data of CH_4, C_2H_6, C_2H_4 as the OCM process hydrocarbons on SAPO-34 molecular sieve. J Ind Eng Chem 2014;20(6):4045–53.
[83] Ng C, Marshall WE, Rao RM, Bansode RR, Losso JN. Activated carbon from pecan shell: process description and economic analysis. Ind Crops Prod 2003;17:209–17. https://doi.org/10.1016/S0926-6690(03)00002-5.
[84] Lima IM, McAloon A, Boateng AA. Activated carbon from broiler litter: process description and cost of production. Biomass Bioenergy 2008;32:568–72. https://doi.org/10.1016/j.biombioe.2007.11.008.
[85] Stavropoulos GG, Zabaniotou AA. Minimizing activated carbons production cost. Fuel Process Technol 2009;90:952–7. https://doi.org/10.1016/j.fuproc.2009.04.002.